

## FIRST SEASON MWA EOR POWER SPECTRUM RESULTS AT REDSHIFT 7

A. P. BEARDSLEY<sup>1,2</sup>, B. J. HAZELTON<sup>3,4</sup>, I. S. SULLIVAN<sup>3</sup>, P. CARROLL<sup>3</sup>, N. BARRY<sup>3</sup>, M. RAHIMI<sup>5</sup>, B. PINDOR<sup>5,6</sup>, C. M. TROTT<sup>7,6</sup>, J. LINE<sup>5,6</sup>, DANIEL C. JACOBS<sup>1</sup>, M. F. MORALES<sup>3</sup>, J. C. POBER<sup>8,3</sup>, G. BERNARDI<sup>9,10,11</sup>, JUDD D. BOWMAN<sup>1</sup>, M. P. BUSCH<sup>1</sup>, F. BRIGGS<sup>12,6</sup>, R. J. CAPPALLO<sup>13</sup>, B. E. COREY<sup>13</sup>, A. DE OLIVEIRA-COSTA<sup>14</sup>, JOSHUA S. DILLON<sup>15,16,17,14</sup>, D. EMRICH<sup>7</sup>, A. EWALL-WICE<sup>14</sup>, L. FENG<sup>14</sup>, B. M. GAENSLER<sup>18,6,19</sup>, R. GOEKE<sup>14</sup>, L. J. GREENHILL<sup>11</sup>, J. N. HEWITT<sup>14</sup>, N. HURLEY-WALKER<sup>7</sup>, M. JOHNSTON-HOLLITT<sup>20</sup>, D. L. KAPLAN<sup>21</sup>, J. C. KASPER<sup>22,11</sup>, HS KIM<sup>5,6</sup>, E. KRATZENBERG<sup>13</sup>, E. LENC<sup>18,6</sup>, A. LOEB<sup>11</sup>, C. J. LONSDALE<sup>13</sup>, M. J. LYNCH<sup>7</sup>, B. MCKINLEY<sup>5,6</sup>, S. R. MCWHIRTER<sup>13</sup>, D. A. MITCHELL<sup>23,6</sup>, E. MORGAN<sup>14</sup>, A. R. NEBEN<sup>14</sup>, N. THYAGARAJAN<sup>1</sup>, D. OBEROI<sup>24</sup>, A. R. OFFRINGA<sup>25,6</sup>, S. M. ORD<sup>7,6</sup>, S. PAUL<sup>26</sup>, T. PRABU<sup>26</sup>, P. PROCOPIO<sup>5,6</sup>, J. RIDING<sup>5,6</sup>, A. E. E. ROGERS<sup>13</sup>, A. ROSHI<sup>27</sup>, N. UDAYA SHANKAR<sup>26</sup>, SHIV K. SETHI<sup>26</sup>, K. S. SRIVANI<sup>26</sup>, R. SUBRAHMANYAN<sup>26,6</sup>, M. TEGMARK<sup>14</sup>, S. J. TINGAY<sup>7,6</sup>, M. WATERSON<sup>7,12</sup>, R. B. WAYTH<sup>7,6</sup>, R. L. WEBSTER<sup>5,6</sup>, A. R. WHITNEY<sup>13</sup>, A. WILLIAMS<sup>7</sup>, C. L. WILLIAMS<sup>14</sup>, C. WU<sup>28</sup>, J. S. B. WYITHE<sup>5,6</sup>

*Draft version June 4, 2016*

### ABSTRACT

The Murchison Widefield Array (MWA) has collected hundreds of hours of Epoch of Reionization (EoR) data and now faces the challenge of overcoming foreground and systematic contamination to reduce the data to a cosmological measurement. We introduce several novel analysis techniques such as cable reflection calibration, high resolution gridding kernels, diffuse foreground model subtraction, and quality control methods. Each change to the analysis pipeline is tested against a two dimensional power spectrum figure of merit to demonstrate improvement. We incorporate the new techniques into a deep integration of 32 hours of MWA data. This data set is used to place a systematic-limited upper limit on the cosmological power spectrum of  $\Delta^2 \leq 2.7 \times 10^4 \text{ mK}^2$  at  $k = 0.27 \text{ h Mpc}^{-1}$  and  $z = 7.1$ , consistent with other published limits, and a modest improvement (factor of 1.4) over previous MWA results. While our result is systematic limited, we identify several strategies to overcome these systematics in future analysis.

*Keywords:* cosmology: observations - cosmology: reionization

<sup>1</sup> Arizona State University, School of Earth and Space Exploration, Tempe, AZ 85287, USA

<sup>2</sup> e-mail: Adam.Beardsley@asu.edu

<sup>3</sup> University of Washington, Department of Physics, Seattle, WA 98195, USA

<sup>4</sup> University of Washington, eScience Institute, Seattle, WA 98195, USA

<sup>5</sup> The University of Melbourne, School of Physics, Parkville, VIC 3010, Australia

<sup>6</sup> ARC Centre of Excellence for All-sky Astrophysics (CAASTRO)

<sup>7</sup> International Centre for Radio Astronomy Research, Curtin University, Perth, WA 6845, Australia

<sup>8</sup> Brown University, Department of Physics, Providence, RI 02912, USA

<sup>9</sup> Square Kilometre Array South Africa (SKA SA), Park Road, Pinelands 7405, South Africa

<sup>10</sup> Department of Physics and Electronics, Rhodes University, Grahamstown 6140, South Africa

<sup>11</sup> Harvard-Smithsonian Center for Astrophysics, Cambridge, MA 02138, USA

<sup>12</sup> Australian National University, Research School of Astronomy and Astrophysics, Canberra, ACT 2611, Australia

<sup>13</sup> MIT Haystack Observatory, Westford, MA 01886, USA

<sup>14</sup> MIT Kavli Institute for Astrophysics and Space Research, Cambridge, MA 02139, USA

<sup>15</sup> Department of Astronomy, UC Berkeley, Berkeley, CA 94720, USA

<sup>16</sup> Radio Astronomy Laboratory, UC Berkeley, Berkeley, CA 94720, USA

<sup>17</sup> Berkeley Center for Cosmological Physics, Berkeley, CA 94720, USA

<sup>18</sup> The University of Sydney, Sydney Institute for Astronomy, School of Physics, NSW 2006, Australia

<sup>19</sup> Dunlap Institute for Astronomy and Astrophysics, University of Toronto, ON M5S 3H4, Canada

<sup>20</sup> Victoria University of Wellington, School of Chemical & Physical Sciences, Wellington 6140, New Zealand

<sup>21</sup> University of Wisconsin-Milwaukee, Department of

Physics, Milwaukee, WI 53201, USA

<sup>22</sup> University of Michigan, Department of Atmospheric, Oceanic and Space Sciences, Ann Arbor, MI 48109, USA

<sup>23</sup> CSIRO Astronomy and Space Science (CASS), PO Box 76, Epping, NSW 1710, Australia

<sup>24</sup> National Centre for Radio Astrophysics, Tata Institute for Fundamental Research, Pune 411007, India

<sup>25</sup> Netherlands Institute for Radio Astronomy (ASTRON), PO Box 2, 7990 AA Dwingeloo, The Netherlands

<sup>26</sup> Raman Research Institute, Bangalore 560080, India

<sup>27</sup> National Radio Astronomy Observatory, Charlottesville and Greenbank, USA

<sup>28</sup> International Centre for Radio Astronomy Research, University of Western Australia, Crawley, WA 6009, Australia

## 1. INTRODUCTION

Detection and characterization of the cosmic dark ages and the Epoch of Reionization (EoR) have the potential to inform our picture of the cosmos in ways analogous to the Cosmic Microwave Background (CMB) over the past several decades. The EoR in particular is rich with both cosmological and astrophysical dynamics as early-universe linear evolution gives way to non-linear structure growth and stars and galaxies reionize the intergalactic medium (IGM).

Several probes are being used to investigate the EoR, but to date, a direct detection eludes researchers. Studies of the polarization of the CMB have placed integrated constraints on the timing of reionization (e.g. Planck Collaboration et al. 2015a,b; Bennett et al. 2013). Meanwhile, observations of highly redshifted quasars have placed upper bounds on redshifts by which reionization is complete. For example, Fan et al. 2006 showed that reionization must be complete by  $z \approx 6$ , a result which was confirmed independent of model by McGreer et al. 2015. Deep optical and infrared galaxy surveys are also beginning to reach the redshifts necessary to further constrain reionization (e.g. Bouwens et al. 2014), and the James Webb Space Telescope will improve on their sensitivity (Gardner et al. 2006).

The 21 cm hyperfine transition from neutral hydrogen residing in the IGM during reionization offers another promising method to study the EoR. Not only is the 21cm signal a *direct* probe of the IGM, but, due to the narrow width of the transition and the relationship between observed frequency and line-of-sight distance, it can be used to map the full three dimensional space of the epoch. (For reviews, see Furlanetto et al. 2006 and Morales & Wyithe 2010.) The first generation of instruments with primary science goals to detect the 21cm EoR signal have been built, including the GMRT (Giant Metrewave Radio Telescope, Paciga et al. 2013), LOFAR (LOw Frequency Array<sup>29</sup>, Yatawatta et al. 2013), PAPER (Precision Array for Probing the Epoch of Reionization<sup>30</sup>, Parsons et al. 2010), and the MWA (Murchison Widefield Array<sup>31</sup>, Tingay et al. 2013). Due to relatively low signal to noise, these instruments aim for a statistical measurement of the EoR in the form of a cosmological power spectrum. Meanwhile, the second generation 21cm EoR machines is on its way with the Hydrogen Epoch of Reionization Array (HERA<sup>32</sup>, D. R. DeBoer, et al. 2016, in prep), which will further refine the power spectrum measurement in early build-out stages, but will ultimately be capable of imaging the ionized bubbles of reionization in its later stages (Beardsley et al. 2015; Malloy & Lidz 2013).

Using the first generation of instruments, several upper limits have been placed on the 21 cm EoR signal (Ali et al. 2015; Dillon et al. 2014; Parsons et al. 2014; Jacobs et al. 2015; Paciga et al. 2013), and Pober et al. 2015 was able to place constraints on physical reionization models. However, much work is to be done to understand the data produced by these arrays. Foreground subtraction and isolation has emerged as a priority in the field.

Central to most analysis strategies is the concept of an “EoR window” – the region of Fourier space where spectrally smooth foregrounds have been isolated from the isotropic (spherically symmetric in Fourier space) cosmological signal (Morales et al. 2006; Bowman et al. 2009). More recent studies have shown the existence of a foreground “wedge”, the result of instrumental mode mixing, throwing power from spectrally smooth foregrounds to higher Fourier modes (Thyagarajan et al. 2015a,b; Trott et al. 2012; Liu et al. 2014a,b; Hazelton et al. 2013; Pober et al. 2013; Vedantham et al. 2012; Morales et al. 2012; Datta et al. 2010). Despite this setback, the EoR window is preserved above the wedge, and the field is pushing forward with several analysis pipelines under active development (e.g. B. J. Hazelton et al. 2016, in prep; D. A. Mitchell et al. 2016, in prep; Jacobs et al. 2016; Trott et al. 2016; Dillon et al. 2013; Trott 2014).

This paper serves two purposes: to demonstrate several new analysis techniques and their impact on power spectrum estimation, and to present the first attempt at a deep integration power spectrum from the MWA. Using a three hour test set of data, we introduce several novel techniques including calibration of cable reflection contamination, high resolution gridding kernels, subtraction of a diffuse foreground model, and development of quality control methods which will be crucial for deeper integrations. We apply these new techniques to a deep integration of data from the first semester of MWA observations (August, 2013 – November, 2013) on a single EoR field and redshift range,  $6.2 < z < 7.5$ . While not expecting to detect the EoR with less than a hundred hours of observations, this intermediate integration will serve to identify and diagnose systematics, allowing for improved analysis in future work.

The remainder of this paper is organized as follows. In Section 2 we briefly describe the MWA instrument and the observations used in this work, in Section 3 we describe our analysis pipeline, in Section 4 we describe several novel techniques in our analysis, in Section 5 we discuss our efforts to apply the analysis pipeline to a deep data integration and compare with a reference pipeline for robust estimation, and we discuss future work in Section 6. Throughout this paper we use a  $\Lambda$ CDM cosmology with  $\Omega_m = 0.73$ ,  $\Omega_\Lambda = 0.27$ , and  $h = 0.7$ , consistent with WMAP seven year results (Komatsu et al. 2011). All distances and wavenumbers are in comoving coordinates.

## 2. THE MURCHISON WIDEFIELD ARRAY AND OBSERVATIONS

The Murchison Widefield Array is one of several first generation radio interferometers with a primary science goal of detecting the 21cm EoR power spectrum. The remote Australian outback offers relative isolation from man-made radio frequency interference (RFI) such as FM radio, or TV stations. A recent study of the RFI environment at the Murchison Radio Observatory can be found in Offringa et al. 2015.

While the 21 cm EoR signal is priority, the MWA is a general observatory serving several science programs beyond cosmology including galactic and extragalactic surveys, time domain astrophysics, solar monitoring, and ionospheric science. The array was thus designed with

<sup>29</sup> <http://www.lofar.org>

<sup>30</sup> <http://eor.berkeley.edu>

<sup>31</sup> <http://www.mwatelescope.org>

<sup>32</sup> <http://reionization.org>

these programs in consideration and the layout was optimized using a pseudo-random antenna placement algorithm (Beardsley et al. 2012) to obtain a well behaved point spread function while retaining a dense core for EoR sensitivity (Beardsley et al. 2013). This is in contrast to more pointed EoR experiments like PAPER, which utilize a highly redundant layout to enhance sensitivity. Redundant arrays can leverage symmetries of the instrument for quick calibration and analysis, but have poor point spread functions, making foregrounds more difficult to characterize. Conversely we use the high imaging capability of the MWA to calibrate and subtract foregrounds based on sky models. A full description of the science capabilities of the array is found in Bowman et al. 2013.

The technical design of the MWA is reviewed in Tingay et al. 2013, and we highlight a few key characteristics that will become important in our analysis of the data. Each antenna of the MWA comprises 16 dual-polarization dipoles placed on a regular grid, lying on a ground screen. The radio frequency signals from these dipoles feed into an analog beamformer which uses physical delays to “point” the antenna. The MWA contains 128 of these antennas, with a tightly packed core of radius 50 m, and extending out to a radius of 1.5 km for higher resolution calibration and imaging.

The beamformed signals (one for each polarization) are then transmitted to receivers in the field, which digitize the signal and perform a first stage coarse frequency channelization of the data (1.28 MHz sub-bands)(Prabu et al. 2015). This channelization applies a filter shape and aliases edge channels, which will later be flagged in our analysis. The observer now selects 24 sub-bands (30.72 MHz total bandwidth) to pass onto the correlator via fiber optic link. The correlator further channelizes the data to 10 kHz resolution, cross multiplies signals between antennas to form visibilities, and averages in time and frequency to a resolution specified by the observer. For the data in this work, the correlator output resolutions were 0.5 seconds in time and 40 kHz in frequency. The data are then written to disk on a cadence of 112 seconds, constituting a single observation, or snapshot.

The EoR observing campaign has adopted a “drift and shift” tracking strategy – we point the telescope towards a sky field of interest, allow the field to drift overhead for about 30 minutes until it begins to leave our field of view, then repoint the instrument at the field. The telescope is thus only pointed at discrete positions, or “pointings”. This tracking is repeated until the field is too low in the sky to track. We have identified three EoR fields relatively devoid of galactic emission and bright extragalactic sources for observing: “EoR0” (RA = 0.00 h, dec =  $-27^\circ$ ), “EoR1” (RA = 4.00 h, dec =  $-27^\circ$ ), and “EoR2” (RA = 11.33 h, dec =  $-10^\circ$ ). In addition, we observe these fields in high and low bands centered at 182 MHz ( $z \approx 6.8$ ) and 154 MHz ( $z \approx 8.2$ ) respectively.

The data for this work includes two sets. First we use a set of 94 high band observations of the EoR0 field from August 23, 2013, which were taken early in telescope operations and found to be particularly well behaved. The MWA EoR collaboration has designated this set as a “golden data set”, which is used to build analysis tools and compare early results. All techniques demonstrated here will use this golden data set. In Section 5 we will use

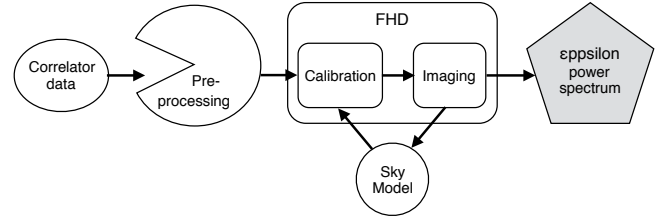


**Figure 1.** Schematic of the analysis pipeline used in this work. The raw correlator data is preprocessed by performing RFI and other flagging. Then the data are calibrated and imaged using an iterative foreground modeling approach with the FHD package. Finally, a power spectrum is formed using the  $\epsilon$ pppsilon package.

a larger data set to move toward a deep integration. This data set consists of all EoR0 high band observations beginning August 23, 2013 (including the golden data set), and concluding when the field was no longer accessible for the season: when the sun was above the horizon for most or all of the field’s transit. The final observation of this set was on November 29, 2013. The individual snapshots are 112 seconds of data at 0.5 second, 40 kHz resolution. In total we analyze 2,780 snapshots, or about 86.5 hours of data.

### 3. ANALYSIS PIPELINE

In order to ensure consistency in analysis, the international MWA EoR collaboration has defined two independent reference analysis pipelines. The details of this strategy are outlined in Jacobs et al. 2016. This study is based on the FHD-to- $\epsilon$ pppsilon pipe, which is in turn based on the Fast Holographic Deconvolution (FHD<sup>33</sup>, Sullivan et al. 2012) and Error Propagated Power Spectrum with Interleaved Observed Noise ( $\epsilon$ pppsilon<sup>34</sup>, B. J. Hazelton et al. 2016, in prep) packages. The general flow of the pipeline is shown in Figure 1, and we give an overview below. As a point of comparison, and to demonstrate robustness of the results, we compute the output power spectra with an independent calibration and power spectrum estimation pipeline, and demonstrate consistency.

#### 3.1. Preprocessing

The preprocessing step converts the data from the non-standard memory dump format from the correlator’s GPUs to a standard UVFITS format (Greisen 2012), performs flagging, averages in time and frequency, and writes to disk. For this step we use the COTTER package (Offringa et al. 2015), which in turn calls the AOFLAGGER<sup>35</sup> to perform RFI flagging (Offringa et al. 2010).

Besides RFI, we manually flag data to remove three other effects. As mentioned in Section 2, the edges of the coarse bands contain high levels of aliasing from the filter applied in the digital receivers. We flag two 40 kHz channels on either side of the coarse band edges (total of four channels per coarse band edge). In principle the aliasing could be calibrated out and these channels could be recovered, but this is left for future work. Second, early data from the MWA also contained some instances where

<sup>33</sup> <https://github.com/EoRIImaging/FHD>

<sup>34</sup> <https://github.com/EoRIImaging/epppsilon>

<sup>35</sup> <http://aoflagger.sourceforge.net/>

antennas were not pointed properly at the beginning of observations due to a beamformer error. This problem has since been resolved, but exists in our data. We therefore flag the first two seconds of each observation to avoid any potentially mis-pointed data. Finally, we flag the central 40 kHz channel of each coarse band. This channel corresponds to the sub-band DC mode, which has been observed to contain anomalous power likely due to very low level rounding errors in the polyphase filter bank of the digital receivers.

In the final step of preprocessing, COTTER averages the data to 2 second, 80 kHz resolution and writes to disk. At this stage each snapshot is contained in a single UVFITS file, which serves as the base unit for calibration and imaging.

### 3.2. Calibration and Imaging

The next step in our pipeline is to calibrate the visibilities. As shown in Figure 1, a sky model is derived from our imaged data, which feeds back into the calibration. This is naturally an iterative process as the sky model is refined with improved calibration solutions. We will describe the sky model in detail in Section 4, but here we present the production mode of analysis after the model has been determined.

Calibration is accomplished within the FHD package in two steps. First we match the raw data to model visibilities formed using a realistic simulation of the array response to our foreground model. This step results in independent complex gains for each antenna, frequency channel, and polarization. In the second step we impose restrictions on these gains motivated by our understanding of the spectral response of the instrument. By reducing the number of free parameters in this step we increase our signal to noise on calibration solutions and avoid absorbing unmodeled confusion source flux into our gain solutions which has been shown to contaminate the EoR window (Barry et al. 2016).

In the first calibration step we allow our complex gains to account for any direction-independent response on a per antenna, per frequency channel, per polarization basis. To define our gains in this way, we have made two simplifications. First we push all direction-dependence of the antenna response into the model of the primary beam. FHD is capable of using separate models for each antenna, though this has not yet been implemented for the MWA due to lack of individual models. The second simplification is to ignore any cross terms between our different axes, for example a mutual coupling between two antennas. In principle these terms would introduce baseline dependent gains, rather than antenna dependent. The MWA has not yet seen evidence of these terms, and so we currently neglect them in our solutions.

Under these assumptions we can express the measured, uncalibrated visibility for an antenna pair  $(i, j)$  as

$$V'_{ij}(\nu) \approx g_i(\nu)g_j^*(\nu)V_{ij}(\nu), \quad (1)$$

where  $g_i(\nu)$  and  $g_j(\nu)$  are the complex gains for antennas  $i$  and  $j$  respectively. Because we are treating polarizations independently, we allow the antenna subscript to run over both East-West (E-W) and North-South (N-S) polarizations.

FHD utilizes the StEFCal algorithm described in

Salvini & Wijnholds 2014 to find the minimum  $\chi^2$  estimate with respect to the complex gains. The result of this operation is estimated gains for every antenna, frequency channel, and polarization. However, with certain known properties of the antenna response we can reduce the number of free parameters in our solution. This takes us to the second step of calibration.

Our initial gain model included an amplitude bandpass common to all antennas,  $B(\nu)$ , and an antenna dependent low order polynomial in frequency. Mathematically we can express our restricted gain as

$$\hat{g}_i(\nu) = B(\nu)P_i(\nu), \quad (2)$$

where the polynomial term can be further decomposed as

$$P_i(\nu) = (A_{i,0} + \nu A_{i,1} + \nu^2 A_{i,2})e^{i(\phi_{i,0} + \nu\phi_{i,1})} \quad (3)$$

The coefficients  $B(\nu)$ ,  $A_{i,n}$ , and  $\phi_{i,n}$  are real quantities. This model allows us to capture arbitrary spectral response due to common antenna factors (such as the polyphase filter shapes or phased array response), as well as slowly varying antenna-dependent deviations. We also found it necessary to include terms dependent on the beamformer to receiver cable length, which we will discuss in Subsection 4.1.

Once all calibration terms are found, we complete the calibration by dividing the raw data by the gain estimates to produce calibrated visibilities. The entire calibration process is done for every snapshot of EoR data, providing both a two-minute resolution time dependence of calibration solutions, as well as model visibilities which are used for foreground subtraction and diagnostic purposes.

After calibration, we form snapshot image cubes (frequency mapping to line-of-sight direction). The visibilities are gridded using the primary beam as the gridding kernel, placing the data in the holographic frame, which has been shown to be the optimal frame for combining images in the sense that it preserves all information for parameter estimation (Morales & Matejek 2009; Bhatnagar et al. 2008). We use a simulation based beam model for MWA antennas developed by Sutinjo et al. 2015. At this stage we also average in frequency by a factor of two by gridding pairs of frequency channels to the same  $uv$  plane, resulting in a frequency resolution of 160 kHz.

The gridded  $uv$  data are then Fourier transformed to create sky-frame images. To avoid aliasing we image out  $90^\circ$  from phase center (gridding resolution of a half wavelength), and crop the image. We found that cropping the image based on beam value resulted in hard edges when integrating images from different snapshots having beams pointed in slightly different directions. To avoid the hard edges, we predetermine a set of HEALPix pixels to interpolate to, and use the same set for all snapshots on a given field. The final cropped field of view for this work is a  $21^\circ$  square centered at RA = 0 h, dec =  $-27^\circ$ .

In principle the foregrounds could be subtracted from the data immediately after calibration, before gridding and imaging. However, for diagnostic reasons, we have found it beneficial to carry the model through the entire pipeline, and only subtract just before squaring to power spectrum units, allowing us to form power spectra of the dirty, model, and residual data.

FHD provides all inputs needed for the  $\epsilon$ ppsipline package, which include weights cubes (for proper accumula-

tion of data), variance cubes (for error propagation), and even/odd interleaved data cubes (for an unbiased estimator and a direct measurement of the noise). We also retain both East-West and North-South polarizations. At this time we can remap our coordinates to cosmological units according to the relationships given in [Morales & Hewitt 2004](#), where angular and frequency units ( $\theta_x, \theta_y, f$ ) map to cosmological distance units ( $r_x, r_y, r_z$ ). Often  $r_z$  is referred to as the line of sight dimension, and denoted as  $r_{\parallel}$ . Similarly,  $(r_x, r_y)$  is the plane perpendicular to the line of sight and is denoted as  $\mathbf{r}_{\perp}$ .

### 3.3. Power Spectra

In the final steps of our pipeline we integrate the snapshot image cubes, and calculate a power spectrum estimate. Though the integration step is formally an imaging component, we conceptually group it with the power spectrum step. This is because all steps of the pipeline up to here have been performed on a per-snapshot basis (no communication between snapshots beyond foreground modeling), and the integration step can be used to select subsets of data for diagnosing power spectrum artifacts. The images produced by FHD are in the holographic frame, which is already properly weighted for combining images, so the integration is simply adding the cubes together, and propagating the weights.

The  $\epsilon$ ppsipline package performs a discrete Fourier transform (DFT) on each  $r_{\parallel}$  slice of the integrated HEALPix cube, forming a cube in  $(\mathbf{k}_{\perp}, r_{\parallel})$ , where  $\mathbf{k}_{\perp}$  represents the cosmological wavenumber in the plane perpendicular to our line of sight, and  $r_{\parallel}$  is the distance to the observed redshift slice along the line of sight. The Fourier transform along the  $r_{\parallel}$  dimension is treated separately due to incomplete  $uv$  sampling and flagged frequency channels, which leads to structure in the frequency sampling along any given  $k_{\perp}$  pixel. We thus adopt the Lomb-Scargle least-squares method to determine the orthogonal eigenfunctions given our sampling function and estimating the total power in each  $k_{\parallel}$  mode ([Scargle 1982](#)). In addition, because the spectrally smooth foregrounds contain vastly more power than the expected EoR signal, we apply a Blackman-Harris window function prior to the  $r_{\parallel}$  to  $k_{\parallel}$  transform. This has the effect of trading off lower effective bandwidth for higher dynamic range.

After squaring and dividing by our observation window function ([Bowman et al. 2006](#)), we arrive in three dimensional power spectrum space. We use the even/odd interleaved cubes to form a signal (odd plus even) and noise (odd minus even) power spectrum, which we subtract from one another to form an unbiased estimate of our signal power. This is mathematically equivalent to cross multiplying the even and odd cubes. The three dimensional power spectrum cube can next be averaged in annuli to form two dimensional power spectra, or spherical shells to form one dimensional power spectra where we will ultimately constrain the EoR.

An example two dimensional residual power spectrum formed from the three hour golden data set is shown in Figure 2. The bulk of the residual power is in the so-called foreground “wedge”, indicated with the diagonal black lines where the solid line corresponds to sky emission at the horizon, and the dashed lines corresponds to

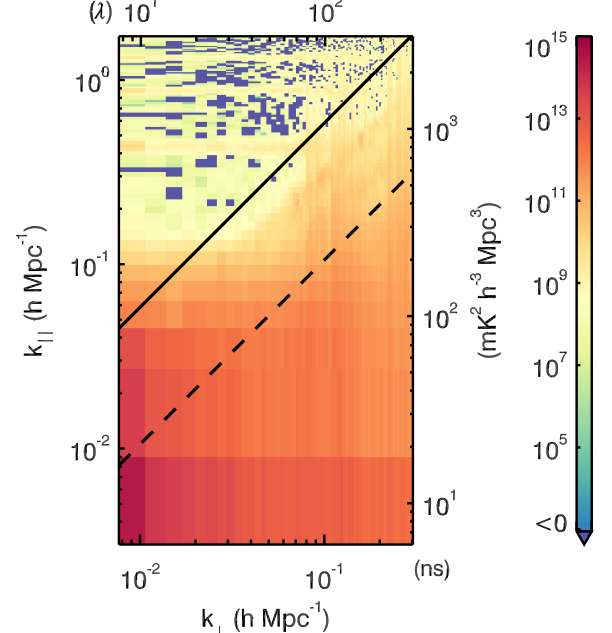


**Figure 2.** An example two dimensional, E-W polarization residual power spectrum formed using the three hour golden data set. The foreground wedge dominates the region below the solid black horizon line, while regions above are mostly noise-like with the exception of horizontal coarse band harmonic lines.

emission at the edge of the MWA field of view. Above the wedge we see horizontal lines of contamination due to the periodic frequency sampling function. These lines are often referred to as the coarse band harmonics. We see vertical streaks at high  $k_{\parallel}$  and high  $k_{\perp}$ . These are due to sparse  $uv$  sampling beyond the dense core of the MWA (starting  $\sim 70\lambda$ ), and the foreground power getting thrown to high spectral modes. Between the coarse band lines and to the left of the vertical streaks we see regions which contain both positive and negative (indicated by blue on the color bar) pixels. These regions are where we have successfully isolated the foregrounds and retained a noise-like EoR window in the three hour integration.

## 4. ANALYSIS METHODS FOR TESTING DATA QUALITY

The two dimensional power spectrum is a useful figure of merit (FOM) as we improve and refine our analysis pipeline. Foregrounds and systematics often manifest with characteristic shapes in this space, enabling us to diagnose problems and quantify improvements ([Morales et al. 2012](#)). We use the MWA 3 hour “golden” data set from August 23, 2013, to repeatedly form power spectra to test and refine our analysis. While an exhaustive catalog of these improvements would be unsuited for this article (and likely bore the reader), we demonstrate the utility of the 2D power spectrum as a FOM with a few key techniques we have employed in our analysis.

### 4.1. Cable Dependent Calibration

Early in our analysis it became apparent that the bandpass of each MWA antenna requires more free parameters than those described in Equation 2. In particular, differing beamformer to receiver cables lead to different bandpass shapes due to signal attenuation. We therefore

allow the amplitude bandpass factor to depend on cable length,  $B_\alpha(\nu)$ , where  $\alpha$  denotes the cable type.<sup>36</sup>

The top panel of Figure 3 shows a 2D power spectrum using the gain model described so far. Three of the horizontal lines in the EoR window can be attributed to the coarse band gaps, as they reside at the harmonics expected for 1.28 MHz periodic sampling. But the sampling cannot account for the fourth line, highlighted by the arrow. The corresponding delay time of the line,  $\tau \approx 1.23 \mu\text{s}$ , corresponds almost exactly to twice the signal travel time through the 150 meter cables (with velocity 0.81c). We therefore introduced a reflection term into our gain model, which allows our restricted gains to account for the interference of the incident signal with a round-trip reflected signal in the cable. A similar approach was taken at lower frequencies in Ewall-Wice et al. 2016. The full gain model is expressed as

$$\hat{g}_i(\nu) = B_\alpha(\nu) (P_i(\nu) + R_i(\nu)), \quad (4)$$

where the reflection term can be further decomposed as

$$R_i(\nu) = R_{i,0} e^{-2\pi i \tau_i \nu}. \quad (5)$$

The reflection coefficient,  $R_{i,0}$  is allowed to be complex, while the reflection delay,  $\tau_i$  is real. After fitting for all other parameters, we fit for the reflection mode. This is done for antennas with suspected reflections, the most offensive of which is seen in the antennas with cables of 150 meters. Because the cables were not cut at exact lengths (variations on order tens of centimeters), we solve for both the reflection coefficient and delay by performing a direct Fourier transform to a highly over resolved delay grid and selecting the mode where the reflection amplitude is largest.

The resulting 2D power spectrum after fitting for cable reflections is shown in the bottom panel of Figure 3, where the reflection line is suppressed below the noise level. This example demonstrates the power of the 2D power spectrum as a figure of merit. The power in the reflection line was about five orders of magnitude below the foregrounds, making it very difficult to detect in image-based metrics. However the power spectrum is specifically designed to be sensitive to low-level spectral structure, and using the two dimensional spectrum allows us to identify the “shape” of contamination, enabling a precise diagnosis.

#### 4.2. Gridding Kernel Resolution

A similar, low level effect which had the potential to contaminate the EoR window is shown in Figure 4. The spectra shown are the *model* spectra – calculated by propagating the sky model visibilities through the entire pipeline. Despite our foreground model not containing spectral structure, the EoR window in the top panel seems to have a floor at a level  $\sim 10^7 \text{ mK}^2 \text{ h}^{-3} \text{ Mpc}^3$ , comparable to predicted EoR signals. In addition there is a faint line in the upper-left of the plot which has the same slope as the wedge, but seems to originate far beyond the horizon.

The source of this floor and super-horizon line was traced to the resolution at which we formed the grid-

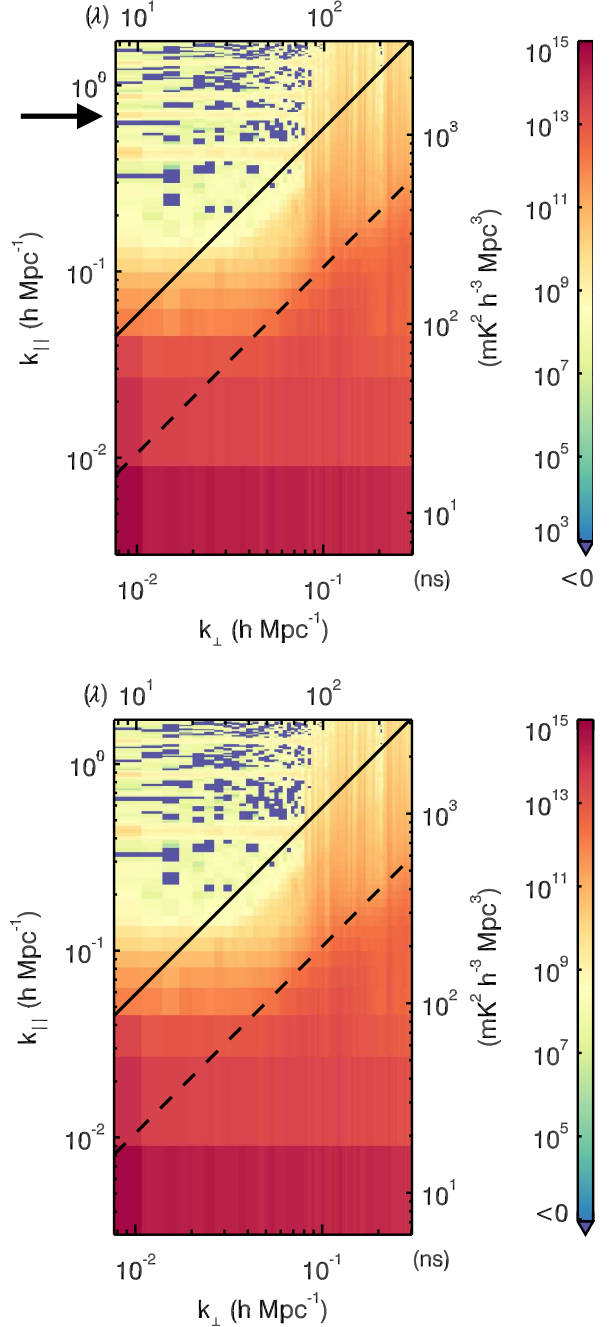


**Figure 3.** Top: Single polarization dirty power spectrum formed from the golden data set, before implementing cable reflection fitting into the calibration loop. The black arrow points to a horizontal band at  $k_{||} \approx 0.7 \text{ h Mpc}^{-1}$ , which cannot be accounted for by the coarse bands. Bottom: After we implement the cable reflection fitting in our calibration solutions, we see the reflection line disappears.

ding kernel when gridding visibilities. In the interest of computational speed and efficiency, the kernel is pre-calculated at a high resolution, then a nearest neighbor lookup table is used to approximate the beam values at discrete pixels. The kernel resolution used in the top panel of Figure 4 was 0.04 wavelengths – much smaller than the half wavelength grid corresponding to horizon to horizon imaging. However, as a baseline migrates in

<sup>36</sup> For logistical purposes the beamformer to receiver cables were installed in six set lengths. Cables of length 90, 150, and 230 meters are RG-6, while 320, 400, and 524 meter cables are LMR400-75.

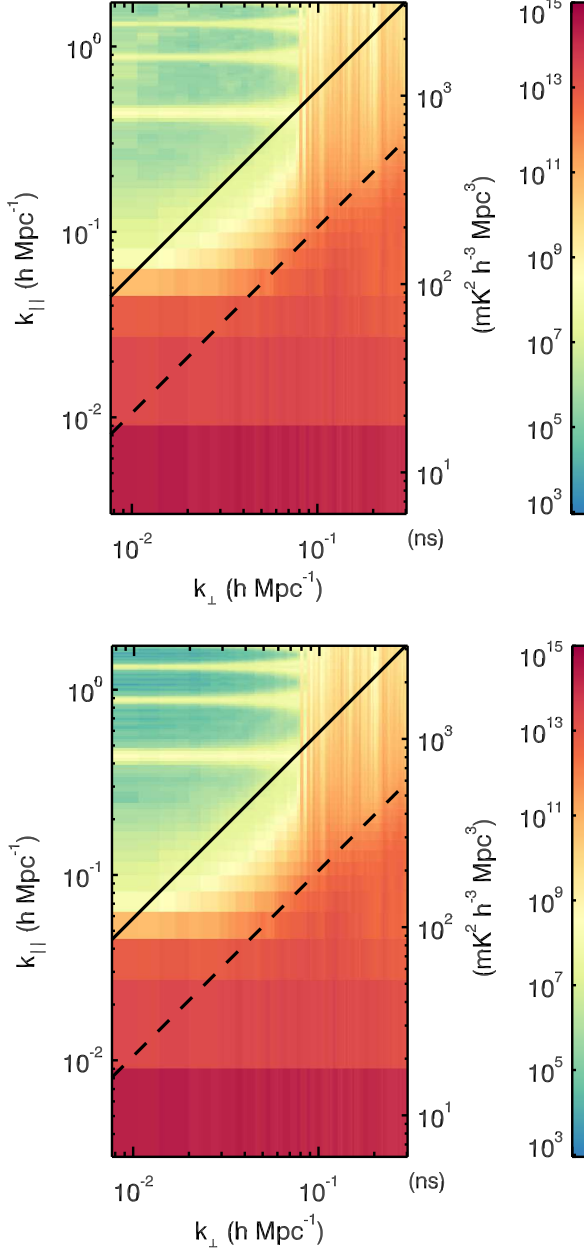


**Figure 4.** *Top:* Single polarization model power spectrum demonstrating the contamination in the EoR window when using insufficient gridding kernel resolution. The window has a floor comparable to an expected EoR signal, and a faint super-horizon line appears at high  $k_{\parallel}$ . *Bottom:* Model power spectrum after increasing the gridding kernel resolution from 0.04 wavelengths to 0.007 wavelengths. The floor is now far below the expected EoR signal level.

uv coordinates across frequencies, it undergoes discrete steps between kernel values used. This effectively results in small baseline position errors which shift periodically in frequency, resulting in power being thrown up into the window and a relatively strong harmonic at the frequency of the shifting (the faint line in the upper left of the window). While we illustrate this effect with a model power spectrum, the same problem exists in the data, but is below the noise levels at three hours of integration.

We resolved this issue by increasing the resolution at

which we form the kernel. While the most accurate answer is to model at infinite resolution, it is not feasible to do so computationally. Instead we chose a resolution at which the effect no longer materially impacts the power spectrum. With experimentation we found a kernel resolution of 0.007 wavelengths was sufficient. The resulting model power spectrum is shown in the bottom panel of Figure 4. The contamination within the EoR window now drops significantly below the predicted cosmological signal levels.

### 4.3. Improving Point Source Model

Our pipeline uses two modes of FHD – the full deconvolution mode to identify point sources and build a catalog, and a production mode where we calibrate using the sky model and subtract it from the data without further fitting. Because full deconvolution on every observation from the MWA is computationally not feasible, we currently restrict ourselves to the golden data set to build our model. The process of building the catalog is presented in P. A. Carroll et al. 2016 (in review). They applied machine learning classification methods to select reliable detections from the full deconvolution FHD mode, culminating in the KGS catalog. The work here uses an early iteration of the KGS catalog that was available at the time of analysis.

It has been shown that subtracting a foreground model strictly within the main lobe of the primary beam will not be sufficient to suppress the power spectrum wedge and unlock the EoR window (Pober et al. 2016; Thyagarajan et al. 2015b,a). In principle we can repeat the model building described above using additional MWA observations pointed away from our field of interest. But until that work is complete we supplement the extent of our point source model using additional catalogs. We accomplish this through a hierarchical catalog pulling from our early KGS catalog, the MWA Commissioning Survey<sup>37</sup> (MWACS, Hurley-Walker et al. 2014), the Culgoora catalog (Slee 1977), and the Molonglo Reference Catalog (MRC, Large et al. 1981). Source fluxes are prioritized in this order based on our confidence in their predicted flux at 182 MHz. We first cluster the source lists to avoid redundant sources, using a 3.5 arcmin neighborhood radius, then select the flux from the highest priority catalog. Spectral indices were obtained from the MWACS and Culgoora catalogs when available, otherwise a two-point spectral index was estimated for Culgoora- MRC matches or MRC-SUMSS matches. All other sources were given a spectral index of -0.8. The spectral index was used to extrapolate the flux from the catalog frequency to 182 MHz, but a uniform spectral index of -0.8 is used within our band when forming model visibilities for calibration and foreground subtraction.

The resulting hierarchical catalog is shown in Figure 5. The EoR0 field corresponds to the red FHD source patch. All sources above the horizon and within a primary beam value greater than 1% maximum (including sidelobes) are included in both our calibration and foreground subtraction models.

To show the effect our hierarchical catalog has on the

<sup>37</sup> The more complete GLEAM Survey (Wayth et al. 2015, Hurley-Walker et al., in collaboration review) was not available at the time of analysis.

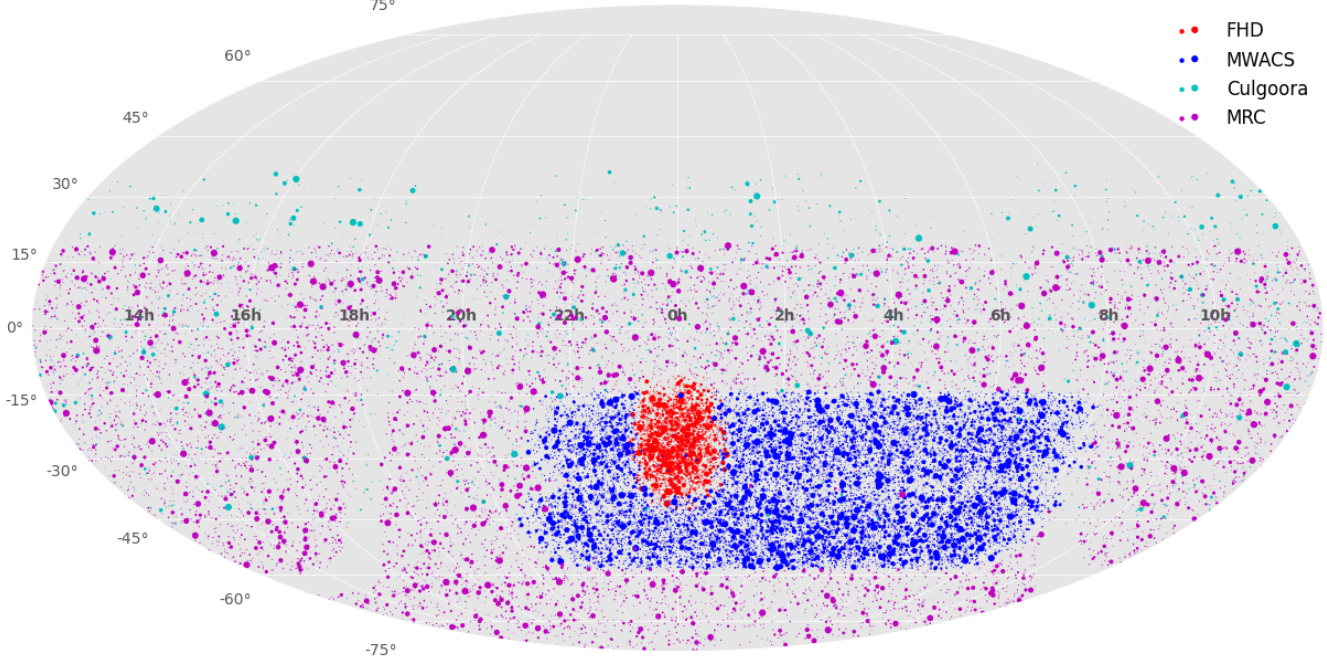


**Figure 5.** Hierarchical catalog used for foreground subtraction. This catalog combines the source lists from our own FHD catalog, the MWACS catalog, Culgoora sources, and the MRC, prioritizing in that order. The EoR0 field corresponds to the red FHD patch, while we use the other catalogs to fill in the sidelobes of the MWA. The size of each dot is proportional to the 182 MHz flux of the source, clipped at 20 Jy.

power spectrum figure of merit, we ran our entire analysis pipeline on the golden data set with two foreground models – first with only the MWACS catalog, and again with the full hierarchical catalog. We then compare the resulting 2D power spectra to inspect whether the new catalog results in more accurate calibration and foreground subtraction.

Because we use the input foreground model to calibrate our visibilities, the gain estimates for our two runs differed. In particular we saw the overall flux scale of the calibrated visibilities was higher when using the full hierarchical catalog. In order to put both residual 2D power spectra onto the same scale for comparison, we first divide each pixel by the corresponding dirty power spectrum pixel, then subtract to arrive at a ratio difference.

$$\text{ratio difference} = \frac{\text{residual}_1}{\text{dirty}_1} - \frac{\text{residual}_2}{\text{dirty}_2} \quad (6)$$

Here we use subscript 1 to represent the MWACS catalog spectra, and 2 for the hierarchical catalog spectra. The ratio difference is shown in Figure 6. The entire wedge being positive (blue) demonstrates that using the new catalog resulted in successfully subtracting higher fractional power. Not only does this indicate we subtract more power, but it also confirms that our calibrated data is more closely matched to the model, meaning that our calibration solutions in general are more accurate.

J. L. B. Line, et al (2016, in review) performed similar analysis, but with an emphasis on the positional accuracy of catalog entries. By using simulations of visibilities they were able to isolate the effect of using perfect versus offset source positions. They confirmed the importance of a complete and accurate point source catalog in order to retain a clean EoR window.

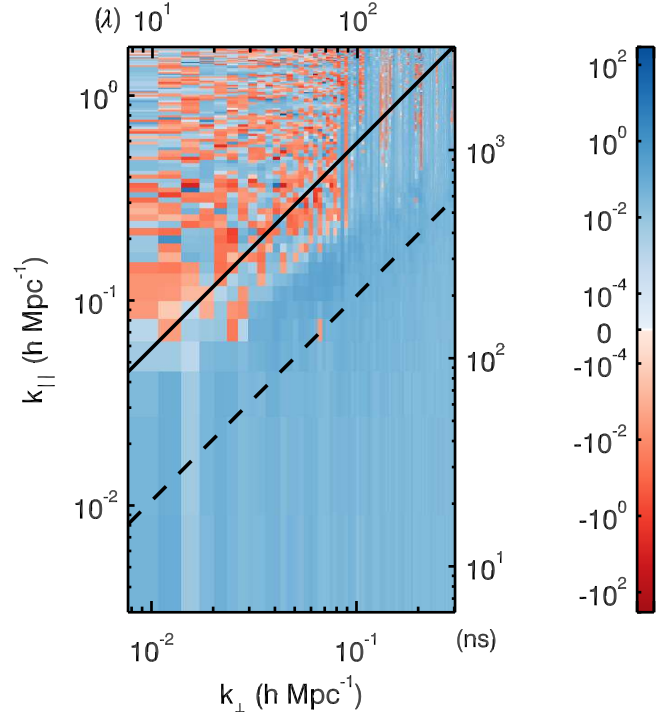


**Figure 6.** Power spectrum ratio difference, according to Equation 6. This metric shows the difference in the fractional E-W residual 2D power spectrum, comparing the MWACS catalog and our hierarchical catalog. By dividing the residual spectrum by the corresponding dirty spectrum before subtracting we remove the effect of the overall flux scale change due to differing calibration solutions. We see that the wedge is completely positive (higher fractional residual when using the MWACS catalog), confirming that the hierarchical catalog subtracts more power from the data. This also reassures that the calibration using the new catalog is more accurate.

#### 4.4. Diffuse Foreground Model Subtraction

In addition to a point source foreground model, we also introduce a diffuse emission model within the primary field of view of the MWA. Though the EoR0 field was chosen to be relatively devoid of galactic emission, we find this diffuse structure still highly contaminating due to the very high sensitivity of the MWA at large scales. For computational purposes we have divided the galactic emission into two regimes – the faint clouds in our main lobe, and the bright plane and other structures in the sidelobes. While the latter has been studied by many people and a Global Sky Model (GSM) is readily available (de Oliveira-Costa et al. 2008), the computational obstacle of simulating the instrument response to a full sky diffuse model is yet prohibitive, though under active pursuit (Thyagarajan et al. 2015b). We instead focus here on diffuse structure within the primary field and leave the full-sky model to future iterations of analysis.

This first iteration of modeling the diffuse structure within our primary field was done by simply using output point-source subtracted residual images of FHD from the three hour golden data set. We combine the images from three hours to leverage the rotation of the earth to improve the point spread function (PSF) of the instrument. This integrating of images is done in a uniformly weighted frame to minimize the effect of double instrument convolution (once when the data is taken, again when we use the output as a model). We then form a pseudo Stokes I image by adding beam-weighted East-West and North-South polarizations. We also integrate in frequency to form a single continuum image for our model. By forcing our model to contain no spectral structure we mitigate the risk of subtracting cosmological signal. Future iterations of this model will contain a spectral index and multiple polarization components.

Ultimately we need model visibilities to subtract from our data. However, rather than storing a model for all observations (different pointings and phase centers), we find it most simple to treat the model as a single HEALPix image which can be used to create model visibilities for each independent observation. FHD treats each pixel in the image as a point source at the pixel location with total flux equal to the flux density of the diffuse image times the area of the pixel and creates model visibilities for each snapshot in the same way that it imports a catalog of point sources.

The diffuse model used for this work is shown in Figure 7. While the actual model image is uniform weighted with resolution  $\sim 6$  arcminutes, we show it smoothed to degree scales to emphasize the large scale structure and approximate what the MWA instrument observes with a natural weight.

For this iteration of analysis we only use the diffuse model for subtraction, and omit it for calibration. At the time of writing short baselines were not producing reliable results in the calibration loop. Instead we chose to omit the diffuse model and mask baselines shorter than 50 wavelengths for calibration purposes. However, we add the diffuse model and unmask short baselines when performing foreground subtraction, and have seen a 90% decrease in total residual power – a strong indication that our diffuse model improves our subtraction. Future iterations will incorporate the model in calibration and

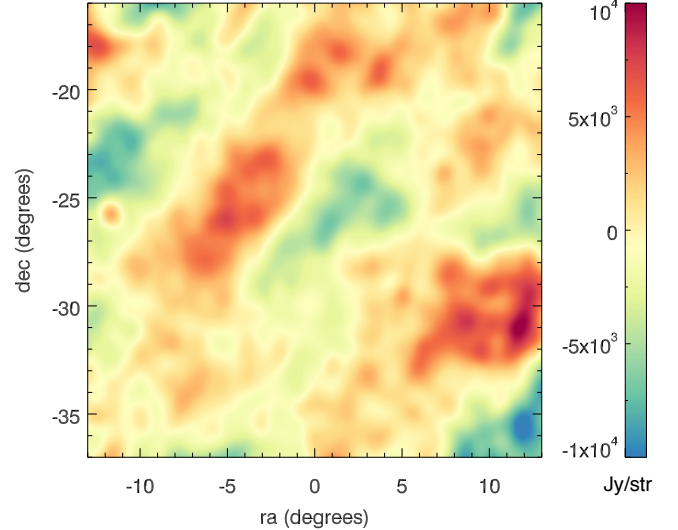


**Figure 7.** The diffuse foreground model within the EoR0 field used for foreground subtraction. This model was created using residual images from the golden data set. The image shown is smoothed to degree scales to emphasize the large scale structure and approximate an MWA snapshot natural weighting. The color scale is in units of Jy/str.

gradually improve the model itself.

We demonstrate the impact of our diffuse model again by running the golden data set through our entire analysis pipeline with and without using the diffuse model. Because the foreground models used for calibration in the two runs are identical (diffuse is omitted for calibration), the calibration solutions were identical and therefore the dirty power spectra were identical as well. We compare the model and residual power spectra by direct subtraction in Figure 8. The top panel shows the model power with the diffuse subtracted from the model power without. The entire plot is negative (red) because we only added power with the diffuse model. Even the EoR window is red (albeit at a much lower level than the wedge) because of power leakage from non-uniform spectral sampling and from the dynamic range limit of the Blackman-Harris window function. The bottom panel is the difference in residual power. The wedge is completely positive (blue), indicating that the diffuse model successfully subtracted from the dirty visibilities. The differences in the window are positive and negative, indicating that the differences in the foreground model in this region are below the three hour noise level.

## 5. A DEEP INTEGRATION

Up to this point we have only discussed testing and analysis on the three hour golden data set. We next turn towards a deep integration, incorporating the techniques described above. We start with all MWA observations taken on the EoR0 field at 182 MHz between August 23, 2013 and November 29, 2013. This includes 2,780 snapshots, or about 86.5 hours of data. We first make data quality cuts, then form power spectra.

### 5.1. Data Selection

All 2,780 snapshots in the data set are preprocessed, calibrated, and imaged using the pipeline described in the previous sections of this article. Similar to tests on

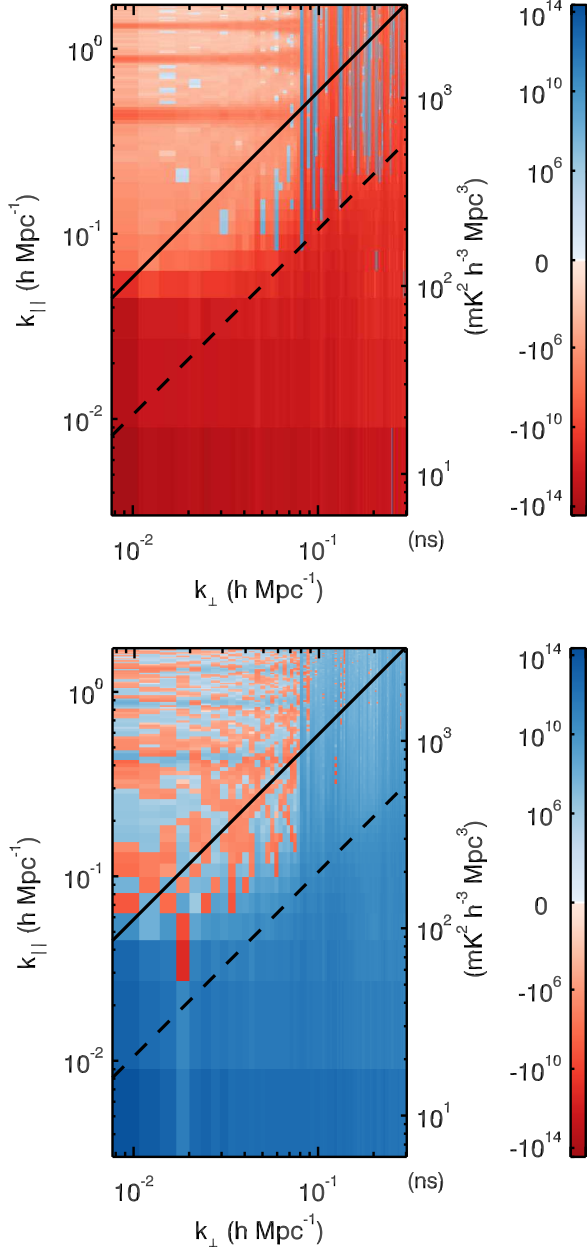


**Figure 8.** Single polarization (E-W) power spectrum differences from the golden data set showing the effect of subtracting a diffuse foreground model. The calibration is identical with and without the diffuse model, so the dirty power spectra are identical. The diffuse model adds a large amount of power to the model (top), and the residual power (bottom) is significantly lower in the wedge when using the diffuse model (positive difference), demonstrating a successful subtraction. While this first attempt at a diffuse model was rudimentary, it shows promise as it successfully removed 90% of the residual power.

the golden data set, we rely heavily on the 2D power spectrum as a diagnostic tool, this time to identify and excise poor quality data.

We use the jackknife method – dividing the data into many subgroups – to filter out bad data and detect patterns. A powerful grouping is to divide the data into the observation day and “pointing” (which direction the antennas were pointed while tracking the EoR0 field). We show an example of one day’s worth of per-pointing

power spectra in Figure 9. The pointings are labeled sequentially with  $-5$  corresponding to five pointing steps prior to zenith transit,  $0$  corresponding to zenith, and  $+4$  corresponding to four steps after zenith. This numbering scheme is shown graphically in Figure 10. Early in the night ( $-5$  through  $-3$ ) the bulk of the galactic plane was still above the horizon, and despite being very far from our primary field of view, highly contaminated our observations through the sidelobes of the instrument. We then have relatively well behaved pointings, with the EoR window dominated by noise, until the final pointing of the night when we can see evidence of the galaxy rising again indicated by strong lines of power at the edge of the foreground wedge. We saw the same contamination on all days of observation and decided to cut all  $-5$ ,  $-4$ ,  $-3$ , and  $+4$  pointings from our data set. In principle it may be possible to model the galactic disk well enough to account for its presence, but with a lack of sufficient galactic model, beam model, and the analysis tools to include it, we leave this to future work.

Motivated by the hand grading done with power spectrum jackknives, we developed another metric to quickly predict power spectrum quality for each snapshot in our data set. We do this by forming a delay spectrum (Parsons et al. 2012) from the raw, uncalibrated visibilities. We then calculate an estimated total EoR window power by integrating the power above the horizon line and below the first coarse band line. While we would ideally use calibrated visibilities for this metric, we have found that the uncalibrated power is strongly correlated to the calibrated power, and the cuts we make below are independent of calibration. This is encouraging because future analysis could use this metric before processing the snapshots, saving valuable computing resources.

We plot the window power for each snapshot in our data set in Figure 11(a). We first note that our conclusion from the jackknife tests is confirmed here – early pointings contain strong contamination and have high window power. We also see many outlier snapshots with excess power. Inspecting power spectra from these individual snapshots confirmed poor data quality, even after calibration. The cause of these contaminants is yet unknown, but could easily be attributed to low-level RFI that was missed by the AOFLAGGER, or intermittent hardware failures. To remove the poor data we made the cut shown with the black box, keeping only snapshots inside.

Next we compare the power in our two instrumental polarizations. When conducting our jackknife tests we saw contamination could exist in one polarization and not the other – potentially due to RFI, or an instrumental failure. We plot the ratio of N-S power to E-W power in Figure 11(b), after applying the previous cut. We see the ratio is generally flat, with the exception of some outliers and almost all of pointing  $+3$ . We suspect that the excess N-S power in the later pointing is due to the galaxy leaking back into the sidelobe of the N-S polarization, but not in the other. Again, we make the cut shown with a black box.

Our final data cut was made when inspecting the residual continuum images output from FHD. We calculate a fractional residual flux RMS in the following way. For each snapshot continuum image, we find the residual flux in the pixels of all sources greater than 0.5 Jy subtracted within half-beam power and scale by the integrated flux

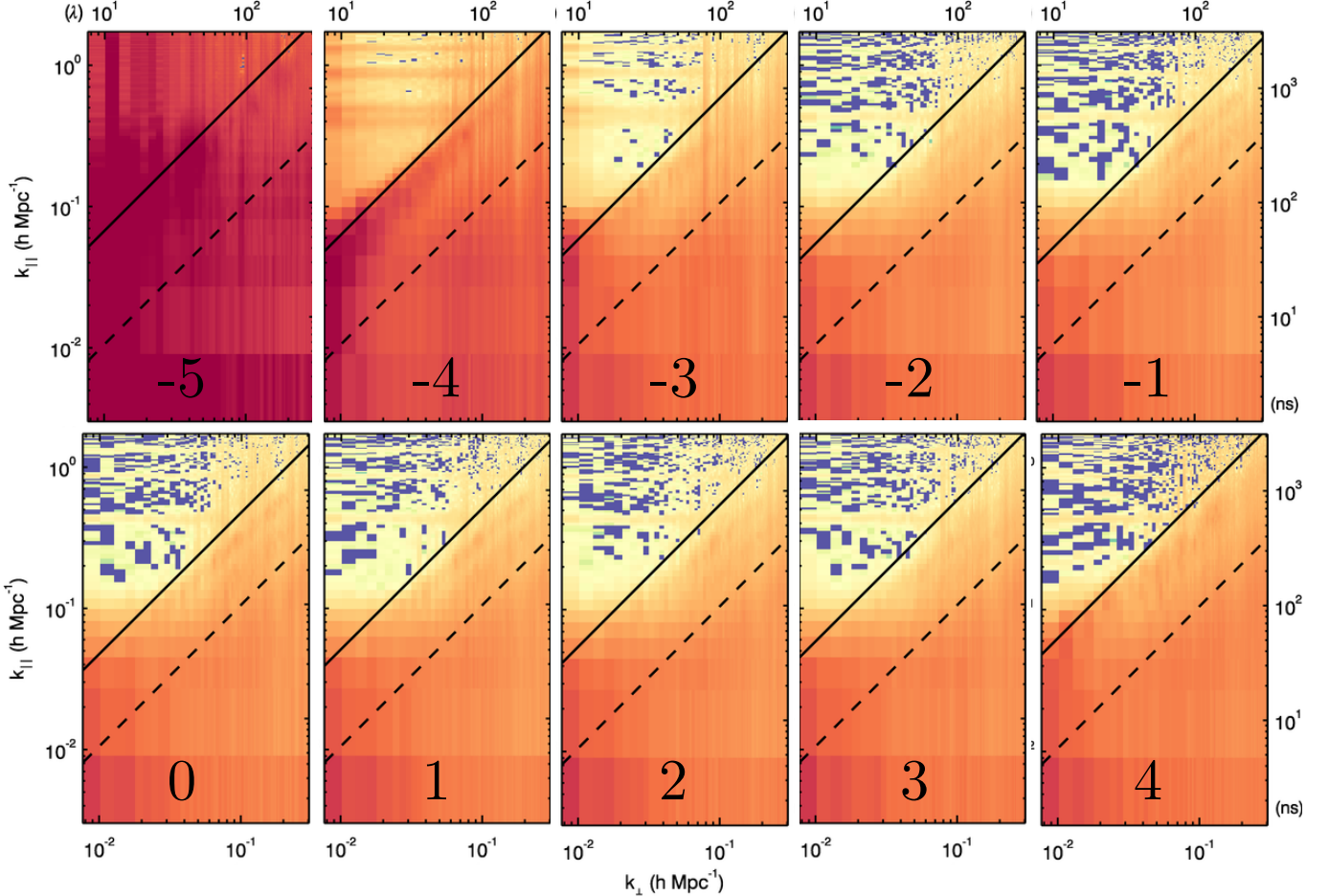


**Figure 9.** An example jackknife test. For this test we divided the data into days and pointings. This is an example array of power spectra (residual E-W polarization) for a single day, August 26, 2013. The early pointings are heavily contaminated by the galaxy in the sidelobes, the window becomes more clear near zenith, and we can see trace contamination at the end of the night (pointing +4) when the galaxy has risen again.

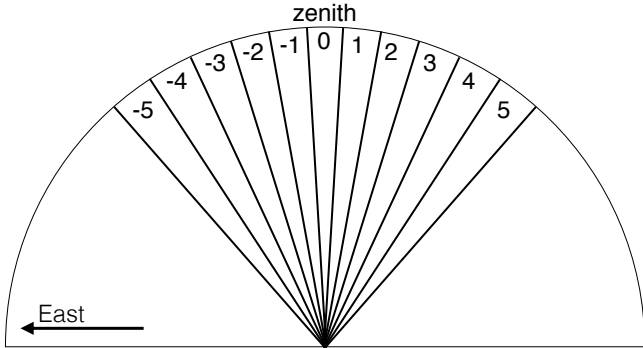


**Figure 10.** This is a cartoon depiction of the numbering scheme used to label pointings in Figures 9 and 11. Looking South, a field transits from the East (left), and the telescope begins observing about 5 pointings before zenith (-5). As the field drifts overhead, we periodically repoint the telescope to recenter the field. Each shift increments the pointing label by one, and the zenith pointing is defined as zero.

of the sources. This gives us a list of fractional residual fluxes for the snapshot, which we then use to calculate an RMS. We found that most snapshots had residual flux RMS  $< 10\%$  with some outliers, which we cut from the data. This cut largely overlapped with previous cuts,

but removed an additional 95 observations. The cause of the high residual flux RMS is yet unknown and is not localized by observation day, LST, pointing, or any other jackknife we have performed.

After the cuts described above, we are left with 1,029 snapshots, or just over 32 hours of data. This is an aggressive cut, with the aim of removing all poor quality data and retaining a clean data set. As mentioned earlier, more sophisticated analysis could allow us to recover data cut from this study in the future (e.g. modeling and removing the galaxy in observations pointing far off zenith).

## 5.2. Results

In this section we discuss the results after processing the remaining 32 hours of data through the  $\epsilon_{\text{ppss}}$  pipeline, and place an upper limit on the EoR power spectrum.

The bandwidth of the MWA and our data set is 30.72 MHz, but in order to avoid the effects of cosmic evolution over the span of our measured redshift range, we limit observations to about 8 MHz, or  $\Delta z \sim 0.4$  at our frequency. We do this by dividing the band into three overlapping sub-bands of 15.36 MHz each, which, after applying the Blackman-Harris window function, will result in effective

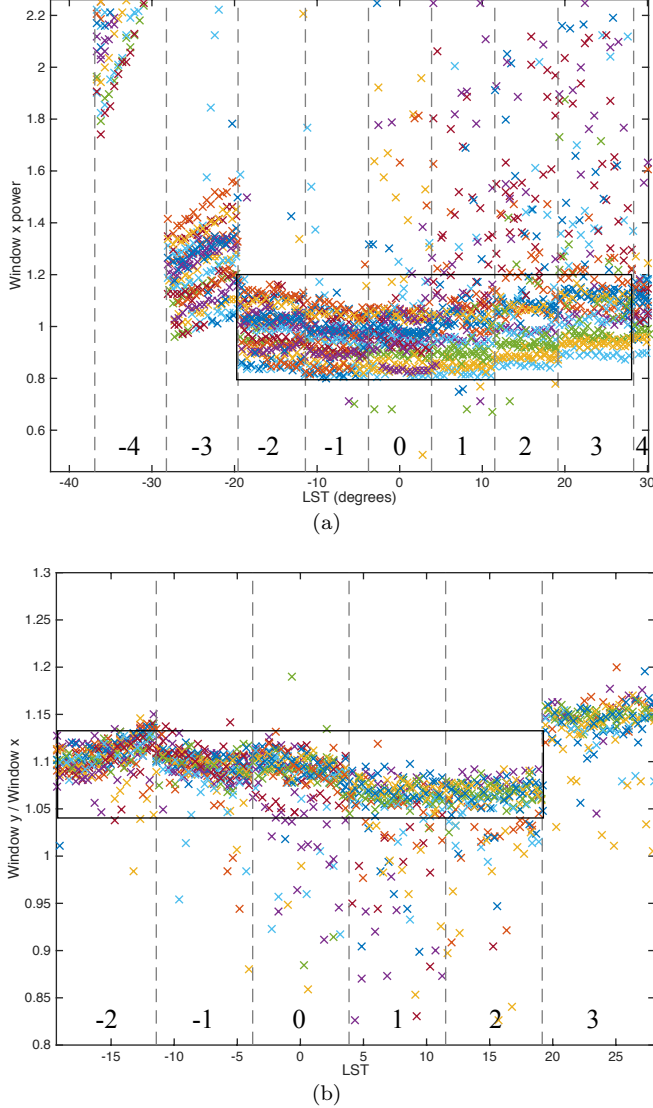


**Figure 11.** *Top:* Window power for each observation in our data set. The window power is calculated from the delay spectrum of uncalibrated data as a fast quality metric. Each color is a distinct day of observing, and the vertical dashed lines represent pointing shifts, with the pointing numbers indicated at the bottom of the plot above the horizontal axis. The black box indicates observations which passed this cut. *Bottom:* Data cut based on window power polarization ratio. For each snapshot that passed the total power cut, we plot the ratio of window powers in the N-S and E-W polarizations. Clear outliers can be seen, including the whole of pointing +3. The black box again indicates the selected data.

bandwidths of 7.68 MHz. We label these sub-bands as “low” ( $z \approx 7.1$ ), “mid” ( $z \approx 6.8$ ), and “high” ( $z \approx 6.5$ ).

The 32 hour integrated residual power spectra for our three sub-bands and both instrumental polarizations are shown in Figure 12. A number of features can be seen in these spectra. In all cases the foreground wedge is prominent, with extra power at large scales (low  $k_{\perp}$ ). This is indication that our diffuse model can improve for deeper subtraction.

The lowest region of the EoR window, above the horizon line and around  $k_{\parallel} \approx 0.25 \text{ h Mpc}^{-1}$ , contains purely positive bins, indicating non-noise-like power. The cause for this seeming leakage is yet unknown, but will ultimately limit our integration in this analysis. One suspected origin of this contamination was individual snapshots with high contamination that slipped through our cuts. However, dividing the data into random subsets and comparing results indicated that there is not a small number of offending observations, instead the leakage appears to exist at a low level in all the data.

Moving up in the window, between the first two coarse band harmonic lines we can see an additional faint line. This is the re-emergence of the 150 meter cable reflections. While the method described in Section 3.2 sufficiently calibrated out this reflection line for the three hour golden set integration, the lower noise level in this deeper integration shows it is not completely removed. Future analysis will require higher signal-to-noise on the reflection fitting, which may require combining snapshots for calibration solutions.

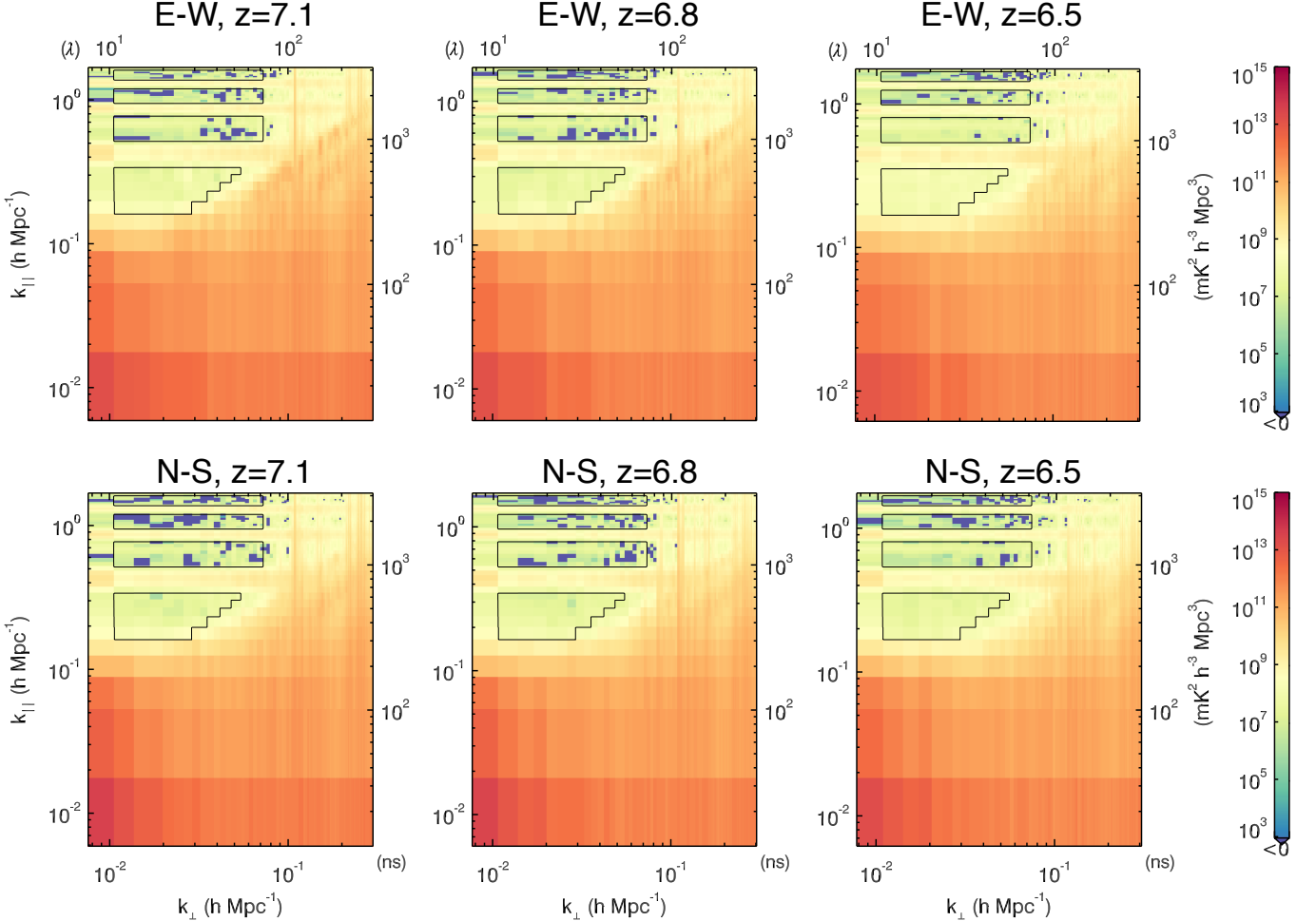
Between the coarse band harmonic lines and the reflection line, we do see regions where our spectra appear noise-like (positive and negative values). This is encouraging despite the leakage at lower  $k_{\parallel}$ , and motivates us to be selective when binning to one dimensional power spectra.

Figure 13 shows slices of power that help isolate the contamination. The two dimensional power spectrum is the N-S, mid band spectrum from Figure 12. We have drawn a horizontal solid blue line to indicate the slice used to plot power as a function of  $k_{\perp}$  for a fixed  $k_{\parallel}$  (top right), and a vertical dashed line to show the slice used to plot power as a function of  $k_{\parallel}$  for a fixed  $k_{\perp}$  (bottom right). In the  $k_{\perp}$  power plot we can see leakage at low and high  $k_{\perp}$ . On the low end this is due to the width of the coarse band harmonics and the exceptionally bright foregrounds at large scales. On the high end we are seeing the residual of the vertical streaks due to poor sampling at large  $uv$ . While the increased noise would mean that we will down weight the bins at large  $k_{\perp}$ , the contamination is even larger, meaning it would bias our estimate even though those bins are down weighted. We exclude bins with  $u < 10\lambda$  and  $u > 70\lambda$ , shown with grey boxes. Between these two regimes are many bins consistent with the noise level, which we include in our one dimensional averages.

Similarly we inspect the  $k_{\parallel}$  power in the bottom right plot of Figure 13. Here we see the huge contamination from foregrounds at low  $k_{\parallel}$ . While the leakage drops significantly, our measurements do not reach the noise level until after the first coarse band harmonic. However, we chose to include bins below the first coarse band with  $k_{\parallel} > 0.15 \text{ h Mpc}^{-1}$  because the cosmological signal is expected to contain substantially higher power at large scales, and ultimately these low  $k_{\parallel}$  bins provide our most competitive limits despite being systematic limited. We exclude the coarse band harmonics by masking out the harmonic bin itself and two bins on either side (total of five bins per harmonic).

The final mask we apply is the wedge. We found that a small buffer beyond the horizon was necessary to completely mask out the wedge, consistent with Dillon et al. 2015. We implement the buffer by extending the horizon line by 15 degrees. This line is shown as the dashed diagonal line in the left panel of Figure 13.

The various masking described above is summarized



**Figure 12.** Residual two dimensional power spectra for the three sub-bands used to place limits on the cosmological signal. The left panels show the low band, centered at 174.7 MHz, or a redshift of 7.1. The middle panels show the mid band, centered at 182.4 MHz, or a redshift of 6.8. The right panels show the high band, centered at 190.1 MHz, or a redshift of 6.5. The contours show the window used for averaging to one dimension.

with the black contours shown on the two dimensional power spectra in Figure 12. The contours show the cuts in two dimensional space, but the masking is actually performed directly in the three dimensional power spectrum cube and averaged directly to one dimension.

The resulting one dimensional power spectra are shown in Figure 14, where the measured power is shown with solid blue, the  $1-\sigma$  noise level is shown with thin red, and the  $2-\sigma$  upper limit for each bin is shown with dashed magenta. Where our unbiased estimator is negative, the absolute value is shown, but with a dotted blue line. For consistency with the literature, we plot our one dimensional power spectra as  $\Delta^2(k) = k^3 P_{21}(k)/(2\pi^2)$ , which has units of  $\text{mK}^2$ .

In all bands and polarizations, we are heavily signal dominated in our most sensitive region (low  $k$ ). This is not surprising based on the 2D spectra we examined earlier. The gaps in the data are due to the excised coarse band harmonics. We can see the cable reflection line between the first two gaps in all polarizations and sub-bands. Between the coarse band harmonic lines, especially at larger  $k$ , are bins which approach the noise level and are consistent with zero (notably the North-South polarization for the low and mid bands). The bin

just above the first coarse band harmonic is also consistent with zero in the low band. These regions are encouraging because they have the potential to continue integrating down with more data. Improved suppression of the coarse band harmonic and cable reflection lines will also improve the limits presented here.

Our best upper limits for a cosmological signal are at low  $k$ , despite the strong leakage. Because any foreground leakage should not correlate with the EoR signal, we can assume that the power of the sum of leakage and cosmological signal is greater than the power of the EoR signal alone, allowing us to set an upper limit. We quote the best  $2-\sigma$  upper limits,  $\Delta_{\text{UL}}^2$ , for each polarization and band in Table 1. These limits and their context in the field are further discussed in Section 6.

### 5.3. Comparison with reference pipeline

As demonstrated in Jacobs et al. 2016, comparison between independent analysis pipelines is essential to evaluate the validity of algorithms under active development. Such comparison provides insight into the strengths and weaknesses of the pipelines, as well as confirmation of results. The analysis discussed so far has been based on the FHD to  $\epsilon$ ppsipline, and here we compare

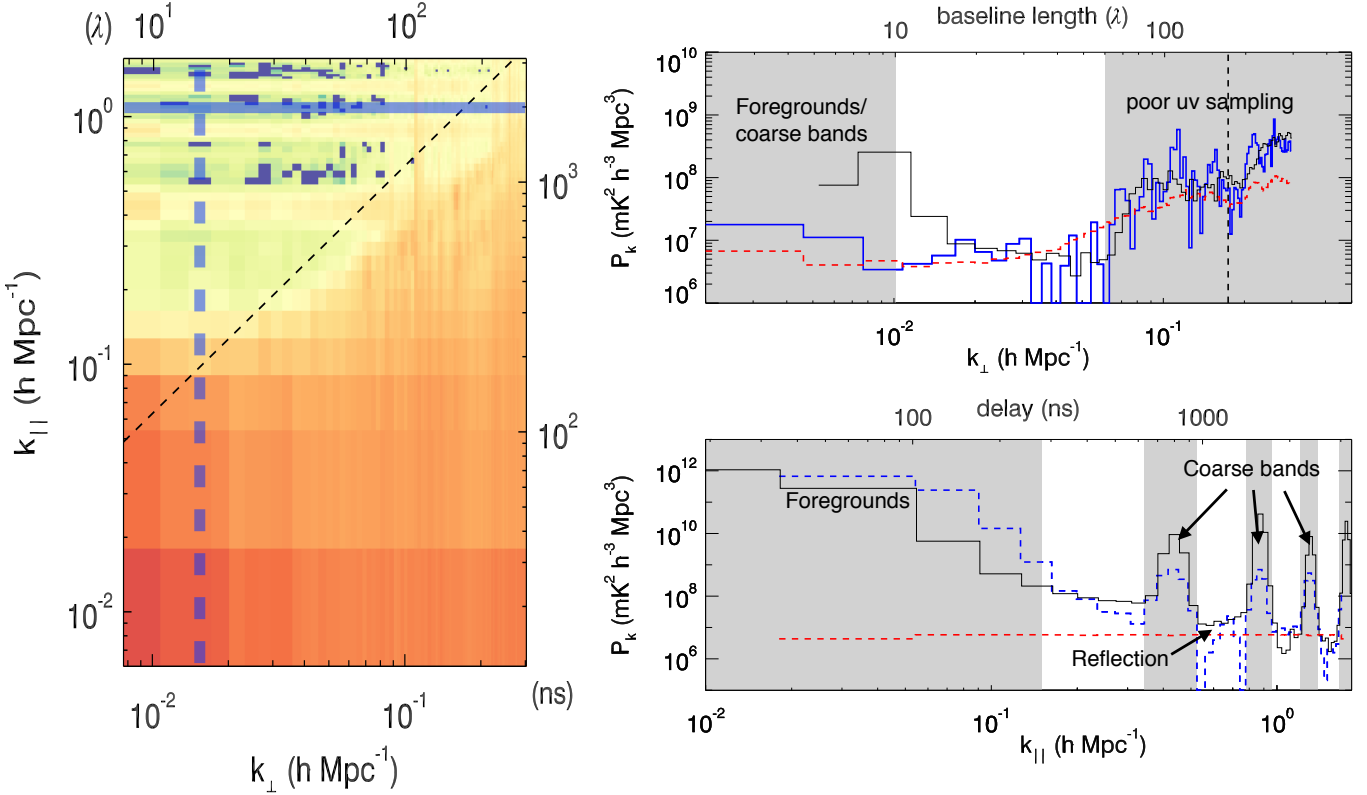


**Figure 13.** *Left:* The N-S,  $z = 6.8$  two dimensional power spectrum repeated from Figure 12. Here we have superimposed blue lines to show slices in  $k_{\perp}$  (solid) and  $k_{\parallel}$  (dashed). *Top right:* Residual power as a function of  $k_{\perp}$  for fixed  $k_{\parallel}$ . The grey boxes show regions which will be excluded from the one dimensional averages. The red dashed line shows the  $1-\sigma$  noise level, and the vertical black dashed line shows the intersection of this slice with the wedge. *Bottom right:* Residual power as a function of  $k_{\parallel}$  for fixed  $k_{\perp}$ . The strong foreground contamination is evident at low  $k_{\parallel}$ , and the coarse band harmonic lines appear as expected. The thin black line in both right panels is the equivalent power slice from the RTS+CHIPS comparison pipeline, which is discussed in Section 5.3.

**Table 1**

Upper limits on the EoR power spectrum for our three sub-bands and two polarizations. Upper limits,  $\Delta_{\text{UL}}^2$ , are at 97.7% confidence level. Cosmological wavenumbers,  $k$ , are in units of  $\text{h Mpc}^{-1}$  and upper limits are in units of  $\text{mK}^2$ . The last two columns, RTS+CHIPS, are produced from the reference pipeline which is discussed in Section 5.3.

Sub-band	$z_0$	Pol	FHD+ $\epsilon$ ppsipline		RTS+CHIPS	
			$k$	$\Delta_{\text{UL}}^2$	$k$	$\Delta_{\text{UL}}^2$
Low	7.1	E-W	0.231	$3.67 \times 10^4$		
Low	7.1	N-S	0.27	$2.70 \times 10^4$	0.16	$3.2 \times 10^4$
Mid	6.8	E-W	0.24	$3.56 \times 10^4$		
Mid	6.8	N-S	0.24	$3.02 \times 10^4$	0.14	$2.6 \times 10^4$
High	6.5	E-W	0.20	$4.70 \times 10^4$		
High	6.5	N-S	0.24	$3.22 \times 10^4$	0.14	$2.5 \times 10^4$

with the Real Time System (RTS, Mitchell et al. 2008; Ord et al. 2010) to Cosmological H I Power Spectrum (CHIPS, Trott et al. 2016) pipeline. Below we present a brief overview of the reference pipeline and highlight lessons learned from the comparison.

The RTS uses a fundamentally different calibration and foreground subtraction approach than FHD, as well as a different input point source model. The primary differences lie in the bandpass calibration, the use of ionospheric corrections, and the lack of a diffuse model. The calibration model uses a model with 1000 sources,

for which ionospheric corrections are estimated and applied, before peeling of those sources from the dataset. The bandpass calibration is fundamentally different to FHD. The bandpass for each antenna is fitted to a 2nd order polynomial within each 1.28 MHz coarse band individually. The delay of the 150 m cable reflection discussed earlier is comparable to the scale of the polynomial fit, so we expect it to naturally be fit out of the gain solutions. Indeed the RTS has not yet seen evidence of the reflection in the processed data (Jacobs et al. 2016). The CHIPS power spectrum estimator applies a full maximum-likelihood estimator to the data. In its full form, the data are weighted by the thermal noise, and a model for the residual point source signal, within a full frequency-dependent description of the instrument. For this comparison, the foreground weighting is not used, in order for a direct comparison with the weighting scheme used by  $\epsilon$ ppsipline.

Of the 1,029 observations calibrated and used by the FHD pipeline, the RTS+CHIPS pipeline successfully calibrated and included 1,003. The remainder failed to calibrate successfully, potentially due to adverse ionospheric conditions. The data were divided into the same three redshift bins, and the 2D and 1D power spectra formed. Table 1 displays comparison 2-sigma upper limits, demonstrating broad consistency between the pipelines. The RTS+CHIPS best limits appear at a lower  $k$  bin than FHD+ $\epsilon$ ppsipline, owing to the different struc-

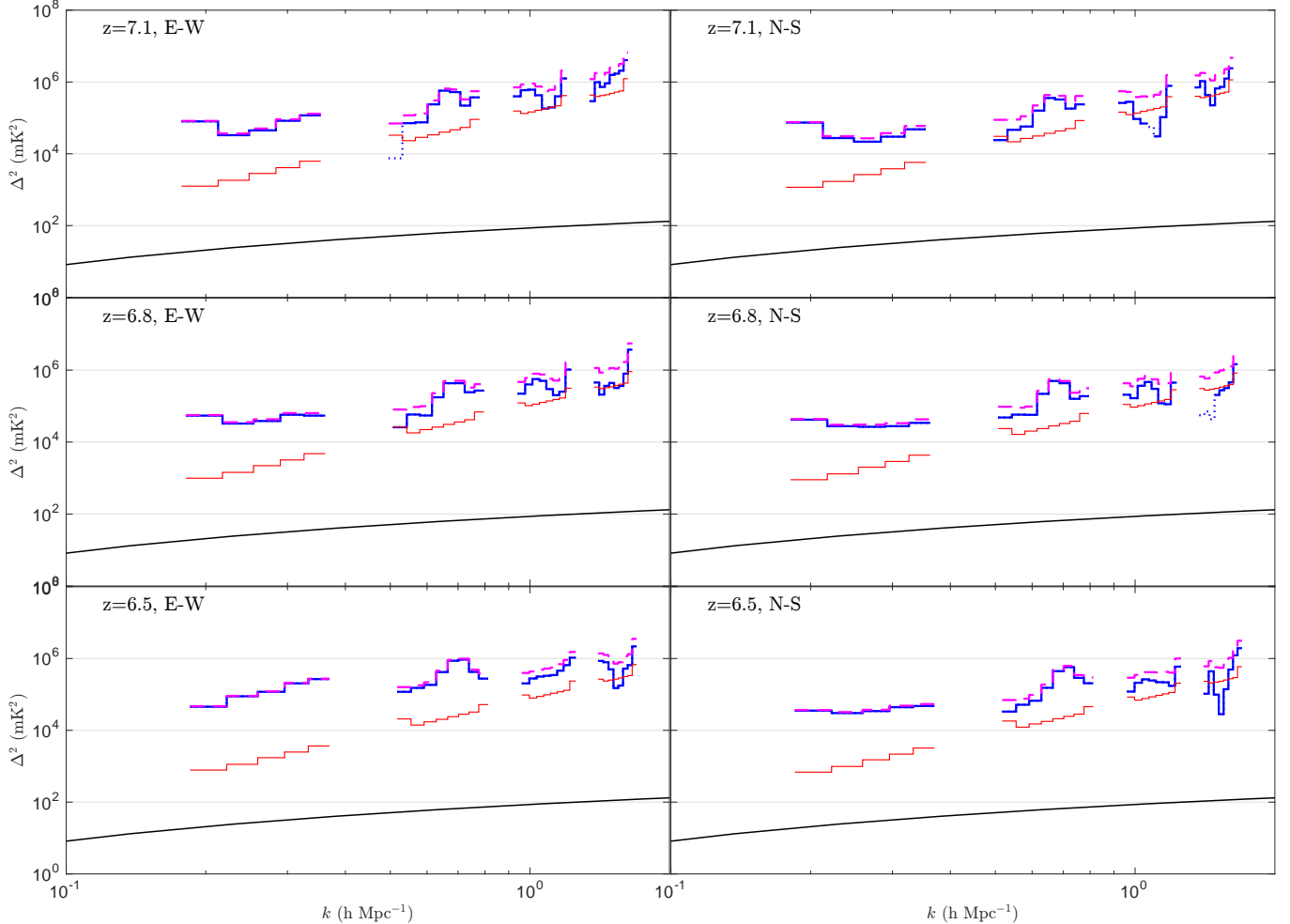


**Figure 14.** One dimensional power spectra for our three sub-bands and both instrumental polarizations. The solid blue line shows the measured power spectrum with step widths corresponding to the bin size used in the average. Where the measured signal is negative we plot the absolute value with a dotted line. The thin red line is the  $1-\sigma$  noise level, and the dashed magenta line is the  $2-\sigma$  upper limit for each  $k$  bin. A fiducial theoretical model for a fully neutral IGM from Furlanetto et al. (2006) is shown in black for reference.

ture of the foreground leakage for the two pipelines. Figure 13, which shows the resulting FHD+ $\varepsilon$ ppsipline slices in  $k_{\parallel}$  and  $k_{\perp}$ , also displays the equivalent power profiles for RTS+CHIPS. The comparison pipeline shows significantly more power at low  $k_{\perp}$ , consistent with no diffuse model being subtracted from the data. Aside from this area, the two pipelines show consistent results. Figure 15 compares the 1D power from both pipelines for the three central redshifts studied in this work. The magenta line reproduces the FHD+ $\varepsilon$ ppsipline results from Figure 14, while the blue line plots the equivalent RTS+CHIPS results (with coarse band harmonics included). Despite the differences in the two pipelines, they produce consistent power across a range of scales, supporting the robustness of the results.

## 6. DISCUSSION

Inspecting our 32 hour integrated power spectra we see two places where we are limited. First there is a region that is leakage-dominated at low  $k$ . The cause of this leakage is yet unknown, but likely due to imperfect calibration, beam models, and/or foreground models. In order to improve on our limit in this regime, future analysis will require calibration which better accounts for

the instrumental response, perhaps by increasing signal to noise through multiple-snapshot solutions or refined antenna response models. Studies of the beam are underway (e.g. Neben et al. 2015), and will likely help to further isolate the foreground contaminates in our power spectra. The foreground model is a constant area of investigation, but improved spectral dependence in both the point source catalog and the diffuse model, as well as the addition of an all-sky galactic model, will continue to improve the foreground subtraction and further unlock the EoR window.

The second limited region in our 1D power spectra is between the coarse band harmonics where our measured signal approaches the noise level. Additional data will likely reduce the noise, and therefore our upper limit, in this regime. However, until the leakage at low  $k$  is understood, progress at higher  $k$  is susceptible to running into the same systematic. While a longer integration may improve the upper limit in the short term, the hope for an eventual detection lies in understanding the contaminants at low  $k$ .

Finally, we place our best upper limits in context with the 21cm EoR field as a whole. A direct comparison

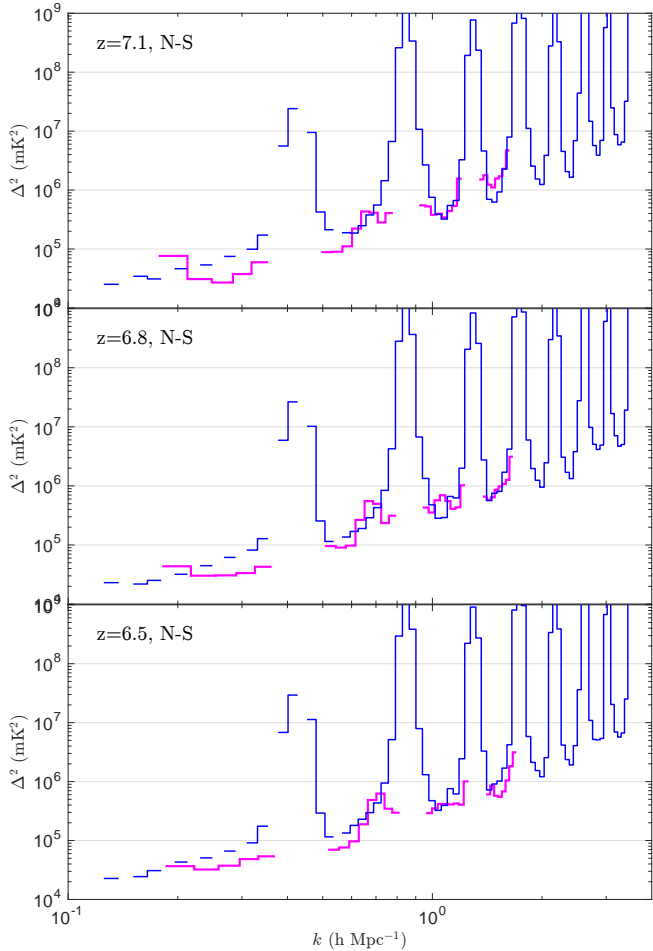


**Figure 15.** Here we compare the upper limits from the FHD+ $\epsilon$  pipeline with those from the RTS+CHIPS pipeline. The magenta lines are repeated from Figure 14, and the blue line is the power plus two sigma thermal error bars line generated by CHIPS. CHIPS does not excise the coarse band harmonic lines, and so we see their strong effect where there are gaps in the magenta lines. The most notable differences are the ability of the RTS+CHIPS pipe to access lower  $k$  modes, while the FHD+ $\epsilon$  pipeline suppresses more power before and after the first coarse band harmonic. While the different analysis methods result in slightly different upper limits, they are generally in agreement.

between measurements from different instruments is difficult due to the varying methods, redshifts, and scales probed. However, if we approximate the power spectrum in units of mK<sup>2</sup> to be roughly flat over the scales probed by the MWA, PAPER, and GMRT, we can glean a view of the current state of the field. The results from this analysis are a modest improvement over the previous best MWA results (Dillon et al. 2015), which is not surprising given that this integration contains about ten times more data, but has a strong signal to noise on the power spectrum. Our results are also consistent with the GMRT limit of  $\Delta^2 \leq 6.15 \times 10^4$  mK<sup>2</sup> at  $z = 8.6$  (Paciga et al. 2013), though probe significantly different periods of the EoR. The frontrunner in terms of an upper limit is the PAPER experiment (Ali et al. 2015; Jacobs et al. 2015; Parsons et al. 2014). The PAPER-64 limit of  $\Delta^2 \leq 502$  mK<sup>2</sup> at  $z = 8.4$  is about one and a half orders of magnitude lower than our best limit in power units, though again probing a significantly different redshift.

While the MWA analysis is not yet at that level of maturity, there is room for rapid improvement. The dashed red line in Figure 14 indicate the noise level possible to reach with this data set if systematics can be overcome.

While this analysis has not reached full potential, it represents the deepest power spectrum integration to date produced by an imaging pipeline. Imaging involves many difficulties (e.g. efficient gridding and mapmaking, foreground modeling), but if systematics can be overcome, it has the potential to quickly compete with other more pointed experiments and analysis styles. Here we have identified a crucial region of power spectrum space that is currently contaminated, with suggestions for improvement in future analysis. With improved calibration techniques, primary beam models, and understanding of foregrounds, the MWA and other imaging analyses will be able to quickly approach the most competitive upper limits in the field.

## 7. ACKNOWLEDGEMENTS

This work was supported by NSF grants AST-1410484 and AST-1206552. DCJ is supported by an NSF Astronomy and Astrophysics Postdoctoral Fellowship under award AST-1401708. This scientific work makes use of the Murchison Radio-astronomy Observatory, operated by CSIRO. We acknowledge the Wajarri Yamatji people as the traditional owners of the Observatory site. Support for the MWA comes from the U.S. National Science Foundation (grants AST-0457585, PHY-0835713, CAREER-0847753, and AST-0908884), the Australian Research Council (LIEF grants LE0775621 and LE0882938), the U.S. Air Force Office of Scientific Research (grant FA9550-0510247), and the Centre for All-sky Astrophysics (an Australian Research Council Centre of Excellence funded by grant CE110001020). Support is also provided by the Smithsonian Astrophysical Observatory, the MIT School of Science, the Raman Research Institute, the Australian National University, and the Victoria University of Wellington (via grant MED-E1799 from the New Zealand Ministry of Economic Development and an IBM Shared University Research Grant). The Australian Federal government provides additional support via the Commonwealth Scientific and Industrial Research Organisation (CSIRO), National Collaborative Research Infrastructure Strategy, Education Investment Fund, and the Australia India Strategic Research Fund, and Astronomy Australia Limited, under contract to Curtin University. We acknowledge the iVEC Petabyte Data Store, the Initiative in Innovative Computing and the CUDA Center for Excellence sponsored by NVIDIA at Harvard University, and the International Centre for Radio Astronomy Research (ICRAR), a Joint Venture of Curtin University and The University of Western Australia, funded by the Western Australian State government.

## REFERENCES

- Ali, Z. S., Parsons, A. R., Zheng, H., et al. 2015, *The Astrophysical Journal*, 809, 61
- Barry, N., Hazelton, B., Sullivan, I., Morales, M. F., & Pober, J. C. 2016, ArXiv e-prints, arXiv:1603.00607
- Beardsley, A. P., Morales, M. F., Lidz, A., Malloy, M., & Sutter, P. M. 2015, *The Astrophysical Journal*, 800, 128
- Beardsley, A. P., Hazelton, B. J., Morales, M. F., et al. 2012, *Monthly Notices of the Royal Astronomical Society*, 425, 1781

- . 2013, Monthly Notices of the Royal Astronomical Society: Letters, 429, L5
- Bennett, C. L., Larson, D., Weiland, J. L., et al. 2013, ApJS, 208, 20
- Bhatnagar, S., Cornwell, T. J., Golap, K., & Uson, J. M. 2008, A&A, 487, 419
- Bouwens, R. J., Bradley, L., Zitrin, A., et al. 2014, ApJ, 795, 126
- Bowman, J. D., Morales, M. F., & Hewitt, J. N. 2006, The Astrophysical Journal, 638, 20, (c) 2006: The American Astronomical Society
- . 2009, The Astrophysical Journal, 695, 183
- Bowman, J. D., Cairns, I., Kaplan, D. L., et al. 2013, PASA - Publications of the Astronomical Society of Australia, 30
- Datta, A., Bowman, J. D., & Carilli, C. L. 2010, The Astrophysical Journal, 724, 526
- de Oliveira-Costa, A., Tegmark, M., Gaensler, B. M., et al. 2008, MNRAS, 388, 247
- Dillon, J. S., Liu, A., & Tegmark, M. 2013, Phys. Rev. D, 87, 043005
- Dillon, J. S., Liu, A., Williams, C. L., et al. 2014, Phys. Rev. D, 89, 023002
- Dillon, J. S., Neben, A. R., Hewitt, J. N., et al. 2015, Phys. Rev. D, 91, 123011
- Ewall-Wice, A., Dillon, J. S., Hewitt, J. N., et al. 2016, MNRAS
- Fan, X., Strauss, M. A., Becker, R. H., et al. 2006, AJ, 132, 117
- Furlanetto, S. R., Oh, S. P., & Briggs, F. H. 2006, Physics Reports, 433, 181, elsevier B.V.
- Gardner, J. P., Mather, J. C., Clampin, M., et al. 2006, Space Sci. Rev., 123, 485
- Greisen, E. 2012, AIPS FITS File Format, AIPS Memo 117
- Hazelton, B. J., Morales, M. F., & Sullivan, I. S. 2013, The Astrophysical Journal, 770, 156
- Hurley-Walker, N., Morgan, J., Wayth, R. B., et al. 2014, PASA - Publications of the Astronomical Society of Australia, 31, 45
- Jacobs, D. C., Pober, J. C., Parsons, A. R., et al. 2015, ApJ, 801, 51
- Jacobs, D. C., Hazelton, B. J., Trott, C. M., et al. 2016, ArXiv e-prints, arXiv:1605.06978
- Komatsu, E., Smith, K. M., Dunkley, J., et al. 2011, The Astrophysical Journal Supplement Series, 192, 18
- Large, M. I., Mills, B. Y., Little, A. G., Crawford, D. F., & Sutton, J. M. 1981, MNRAS, 194, 693
- Liu, A., Parsons, A. R., & Trott, C. M. 2014a, Phys. Rev. D, 90, 023018
- . 2014b, Phys. Rev. D, 90, 023019
- Malloy, M., & Lidz, A. 2013, The Astrophysical Journal, 767, 68
- McGreer, I. D., Mesinger, A., & D'Odorico, V. 2015, MNRAS, 447, 499
- Mitchell, D., Greenhill, L., Wayth, R., et al. 2008, Selected Topics in Signal Processing, IEEE Journal of, 2, 707
- Morales, M., & Wyithe, J. 2010, Annual Review of Astronomy and Astrophysics, 48, 127
- Morales, M. F., Bowman, J. D., & Hewitt, J. N. 2006, The Astrophysical Journal, 648, 767, (c) 2006: The American Astronomical Society
- Morales, M. F., Hazelton, B., Sullivan, I., & Beardsley, A. 2012, ApJ, 752, 137
- Morales, M. F., & Hewitt, J. N. 2004, The Astrophysical Journal, 615, 7, (c) 2004: The American Astronomical Society
- Morales, M. F., & Matejek, M. 2009, Monthly Notices of the Royal Astronomical Society, 400, 1814
- Neben, A. R., Bradley, R. F., Hewitt, J. N., et al. 2015, Radio Science, 50, 614
- Offringa, A. R., de Bruyn, A. G., Biehl, M., et al. 2010, Monthly Notices of the Royal Astronomical Society, 405, 155
- Offringa, A. R., Wayth, R. B., Hurley-Walker, N., et al. 2015, PASA - Publications of the Astronomical Society of Australia, 32
- Ord, S. M., Mitchell, D. A., Wayth, R. B., et al. 2010, Publications of the Astronomical Society of the Pacific, 122, 1353
- Paciga, G., Albert, J. G., Bandura, K., et al. 2013, Monthly Notices of the Royal Astronomical Society, 433, 639
- Parsons, A. R., Pober, J. C., Aguirre, J. E., et al. 2012, The Astrophysical Journal, 756, 165
- Parsons, A. R., Backer, D. C., Foster, G. S., et al. 2010, The Astronomical Journal, 139, 1468
- Parsons, A. R., Liu, A., Aguirre, J. E., et al. 2014, ApJ, 788, 106
- Planck Collaboration, Aghanim, N., Arnaud, M., et al. 2015a, ArXiv e-prints, arXiv:1507.02704
- Planck Collaboration, Ade, P. A. R., Aghanim, N., et al. 2015b, ArXiv e-prints, arXiv:1502.01589
- Pober, J. C., Parsons, A. R., Aguirre, J. E., et al. 2013, The Astrophysical Journal Letters, 768, L36
- Pober, J. C., Ali, Z. S., Parsons, A. R., et al. 2015, The Astrophysical Journal, 809, 62
- Pober, J. C., Hazelton, B. J., Beardsley, A. P., et al. 2016, ApJ, 819, 8
- Prabu, T., Srivani, K., Roshi, D., et al. 2015, Experimental Astronomy, 1
- Salvini, S., & Wijnholds, S. J. 2014, A&A, 571, A97
- Scargle, J. D. 1982, ApJ, 263, 835
- Slee, O. B. 1977, Australian Journal of Physics Astrophysical Supplement, 43, 1
- Sullivan, I. S., Morales, M. F., Hazelton, B. J., et al. 2012, The Astrophysical Journal, 759, 17
- Sutinjo, A., O'Sullivan, J., Lenc, E., et al. 2015, Radio Science, 50, 52
- Thyagarajan, N., Jacobs, D. C., Bowman, J. D., et al. 2015a, The Astrophysical Journal Letters, 807, L28
- . 2015b, The Astrophysical Journal, 804, 14
- Tingay, S. J., Goeke, R., Bowman, J. D., et al. 2013, PASA - Publications of the Astronomical Society of Australia, 30
- Trott, C. M. 2014, PASA - Publications of the Astronomical Society of Australia, 31, 26
- Trott, C. M., Wayth, R. B., & Tingay, S. J. 2012, The Astrophysical Journal, 757, 101
- Trott, C. M., Pindor, B., Procopio, P., et al. 2016, ApJ, 818, 139
- Vedantham, H., Shankar, N. U., & Subrahmanyam, R. 2012, The Astrophysical Journal, 745, 176
- Wayth, R. B., Lenc, E., Bell, M. E., et al. 2015, PASA - Publications of the Astronomical Society of Australia, 32, e025
- Yatawatta, S., de Bruyn, A. G., Brentjens, M. A., et al. 2013, Astronomy and Astrophysics, 550, A136